Chapter 2

Anisotropy in 2 dimensions

No man of honor makes elastic constants equal. – K. Helbig, 1990

The goal of the first three chapters of this thesis is to build up an intuition of how wave propagation works in anisotropic media. In this chapter we cover the simplest case, two-dimensional anisotropy. Because it is an extremely symmetric special case, two-dimensional anisotropy is somewhat misleading. Nevertheless it is the first logical step away from isotropy, and forms a necessary basis for the discussion of three-dimensional anisotropy to follow in Chapter 3.

2.1   Elliptical anisotropy[1]

The simplest kind of two-dimensional anisotropy is elliptical anisotropy. A medium is *elliptically anisotropic* if wavefronts spreading away from a point source are ellipses rather than circles.

Technically this isn't a proper definition; anisotropy is an inherent fundamental quality of a medium that only secondarily manifests itself in observable behaviors. However, true three-dimensional multi-component elliptical anisotropy does not even fit into any of the handful of physically allowed anisotropic symmetry systems (see section 2.1.2 for an

---

[1]This section is modified and extended from "Imaging reflections in elliptically anisotropic media" (1988).
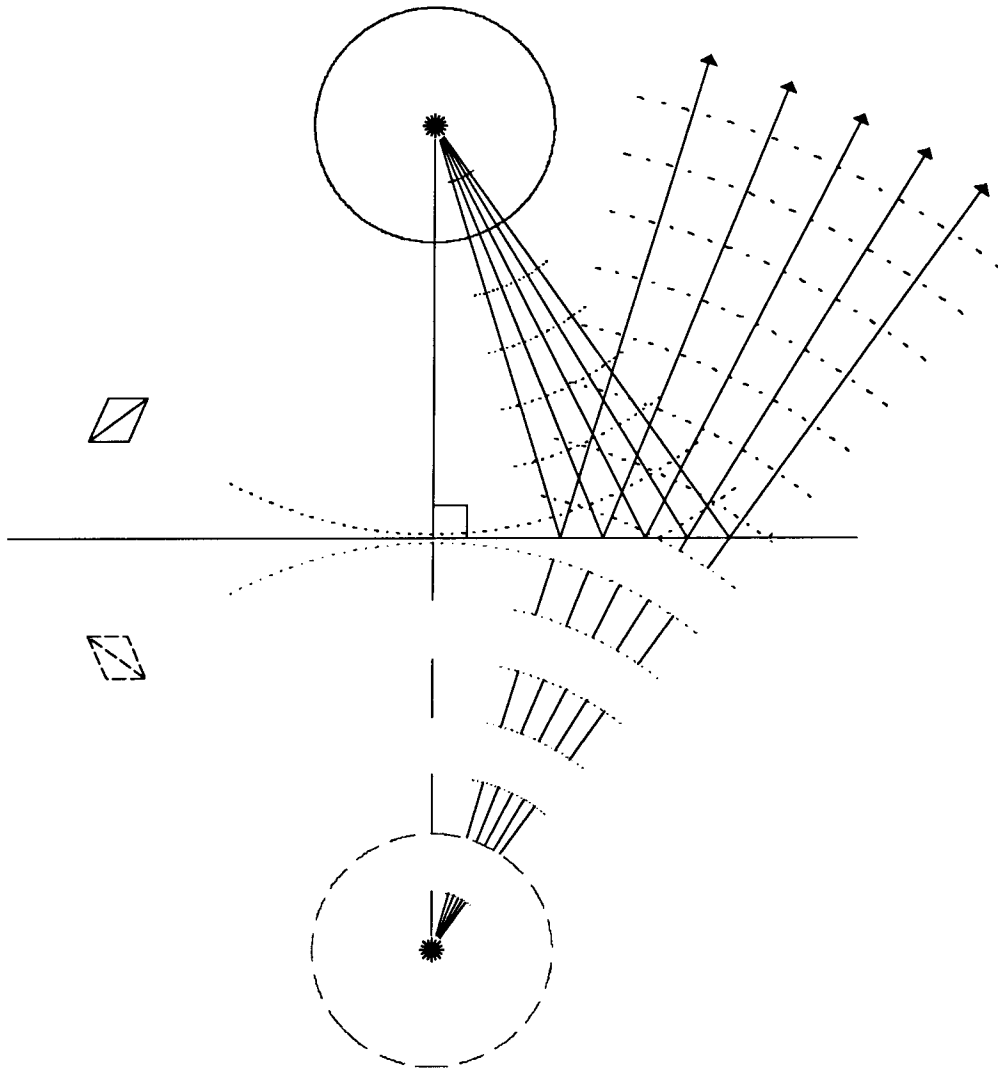
FIG. 2.1. A mirror in an isotropic medium. The starburst above the mirror represents a point source. One complete wavefront and several partial ones are shown propagating away from it, along with some associated rays. Below the mirror we see virtual images of objects above the mirror.
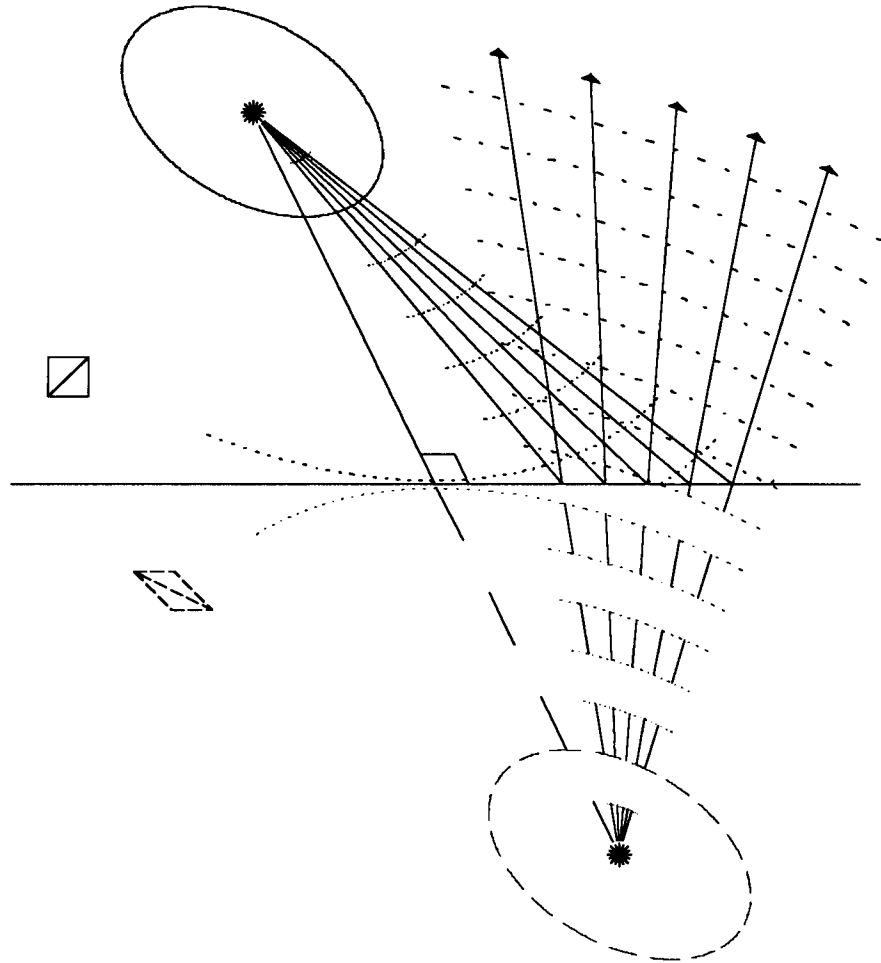
FIG. 2.2. A mirror in an elliptically anisotropic medium. It is just Figure 2.1 stretched and rotated (linearly transformed). Note that while the image of the point source (the starburst) is also a point, the image of the square on the left is a strongly sheared parallelogram.

explanation of why this should be so)! This is all right, because this kind of anisotropy is not meant to model how real wavefronts should behave anyway. Elliptical anisotropy is mostly useful as the logical next level of approximation above complete isotropy.[2]

2.1.1 Stretching Isotropy

An ellipse is just a flattened circle; similarly, if we "flatten" the isotropic wave equation by linearly transforming the spatial coordinates, we get an elliptically anisotropic wave equation. We can illustrate the properties of elliptical anisotropy graphically by showing linearly transformed isotropic wavefields.

A graphical illustration

A "snapshot" shows a wavefield at one instant of time. Since stretching a snapshot of a wavefield is the same as linearly transforming the spatial coordinates, we can get a snapshot of an elliptically anisotropic wavefield by simply stretching the corresponding isotropic snapshot. As an illustration, we examine the case of a virtual image created by a mirror.

In Figure 2.1 we show the standard isotropic case. The starburst at the top of the picture represents a point source, and the starburst at the bottom of the picture is its virtual image. If we stretch Figure 2.1 at a 45° angle to the reflector, and then rotate it so that the reflector is again horizontal, we obtain Figure 2.2. (Remember that rotation is also a linear transformation.) This new figure must show how a mirror in an elliptically anisotropic medium works. (Since the starbursts are supposed to represent *point* sources, they are not stretched.)

Examining the two figures we can see that the "mirror image" of the point source is a point in both cases. The "mirror image" of the square near the left edge in Figure 2.2, however, is not a square but a strongly sheared parallelogram.

What implications does this have for migration? Since each point above the mirror maps into a perfect point below the mirror, isotropic migration must still be able to *focus* the image perfectly. However, we can also see by looking at the image of the square that even though the image is in focus it is "stretched". If we want a true depth picture we have to "unstretch" the image.

---

[2]If you *insist* on a physical model, the SH wave in transversely isotropic media is the best available. This mode will be briefly discussed on page 20.

Mathematical analysis

Any elliptically anisotropic acoustic wave equation can be written in the form

$$(1 + \kappa_1^2)\frac{\partial^2 \phi}{\partial x^2} + 2\kappa_1\kappa_2\frac{\partial^2 \phi}{\partial xz} + \kappa_2^2\frac{\partial^2 \phi}{\partial z^2} = c^{-2}\frac{\partial^2 \phi}{\partial t^2}, \tag{2.1}$$

where ϕ is the field variable, and κ_1, κ_2, and c determine the medium properties.

How do we migrate data recorded over an earth that satisfies this equation? If we assume the data were recorded on the surface ($z = 0$), then any transformation that leaves time and $z = 0$ unchanged will likewise leave the data unchanged. The linear transformation

$$\begin{aligned} x &= x' + \kappa_1 z' \\ z &= \kappa_2 z' \end{aligned} \tag{2.2}$$

leaves time and $z = 0$ unchanged and also simplifies equation (2.1) to

$$\frac{\partial^2 \phi}{\partial x'^2} + \frac{\partial^2 \phi}{\partial z'^2} = c^{-2}\frac{\partial^2 \phi}{\partial t^2}. \tag{2.3}$$

This is just the standard isotropic acoustic wave equation. Since it fits the surface data exactly, it can be used to focus our data as well as the correct equation (2.1). If we then apply equation (2.2) to map the image back to the correct coordinates, we will have correctly migrated the data.

Multiple Layers

The same stretching principle extends to the case of multiple layers. Each layer must be independently stretched to become isotropic, stretching must be consistent across layer boundaries, and the surface must remain unchanged. To accomplish this, start at the surface and stretch all the layers beneath, making the first layer isotropic and leaving the surface fixed. Proceed to the top of the second layer. Treat this as the new "surface," and stretch all the layers beneath again to make the second layer isotropic. Continue down in this way through all the layers. Each stretching step leaves the surface data unchanged, maintains continuity across layer boundaries, and makes another layer isotropic. Figure 2.3 illustrates this stretching process for a two layer model.

Just as for a single layer, an isotropic migration with the correct velocities will focus
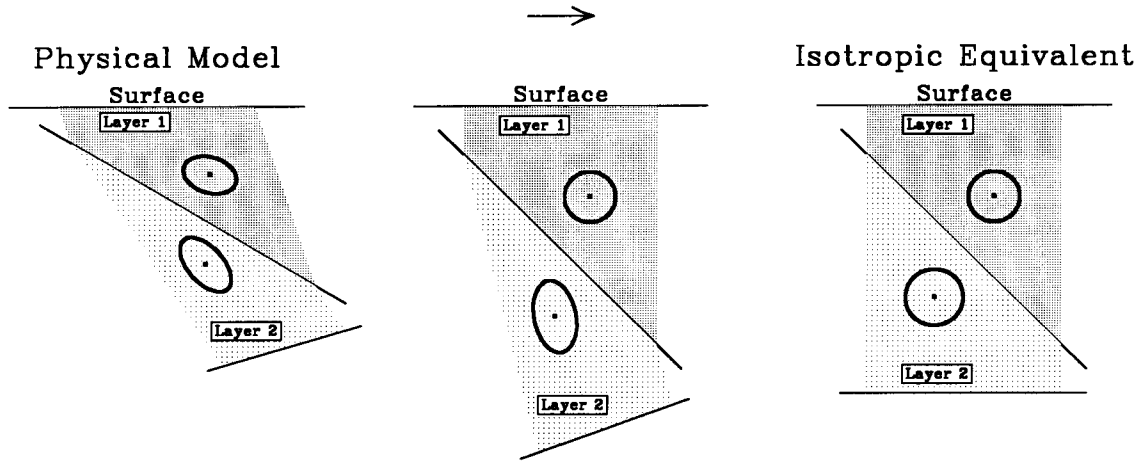
FIG. 2.3. Converting a two layer physical model to its isotropic equivalent. A wavefront radiating from a point source is shown in each layer. If the layer is isotropic, the wavefront is circular. On the left is the true depth picture. On the right is the picture that standard processing would infer from surface data alone using an isotropic assumption. Note the bottom interface appears horizontal, even though it actually dips to the left. The middle panel shows the conversion process after stretching the first layer.

the data, but a second layer-by-layer linear transformation may be necessary to map the focused image to true depth.

This simple stretch concept has a curiously irregular record in the literature. Blair and Korringa (1987) and Meadows (1985) present analogues of equation (2.2), but address only the single-layer case. Helbig (1983) discusses the multi-layer case in some detail, but considers only stretching perpendicular to layer boundaries (missing the possibility of $\kappa_1 \neq 0$). One of the primary source papers on elliptical anisotropy (Levin, 1978) gets the $\kappa_1 \neq 0$ case wrong.

2.1.2 Does elliptical anisotropy have meaning?

So far we have managed to discuss elliptic anisotropy without considering the realities imposed by physics. Does stretching have meaning? The standard elastic wave equation cannot be stretched, because the orthogonality of particle motion between wave types would be lost in the process.

There is one interesting special-case exception to this rule. It is possible to stretch SH waves propagating in a symmetry plane. The two-dimensional scalar SH wave equation can be linearly transformed and remain a physically valid wave equation, because the

particle-motion direction of the single uncoupled SH wavetype remains perpendicular to the two-dimensional plane, unaffected by any stretching within the plane. Thus in an ideal SH reflection survey there is theoretically no way to tell an isotropic earth from an elliptically anisotropic one. The recorded wavefield and the particle motion in the stretched and unstretched cases are exactly the same; the "stretch" is both kinematically and dynamically correct.

Schoenberg and Costa (submitted) discuss this special case. While they allow the elliptical anisotropy to have an arbitrary orientation, they limit their analysis to the case of flat-layered media. This raises a subtle question: in Figure 2.3 we saw that unstretching the elliptical anisotropy in each layer also changed the relative orientations of the layer boundaries. How do they perform the unstretching without generating tilted layers? Their special flat-layer case works because all the layer boundaries in their examples start out flat and parallel. Linear transformations leave parallel lines parallel. Since the surface layer remains fixed and flat, at every step of their layer-by-layer unstretching process all the layer boundaries must also remain flat.

We have seen that the stretch can be exact in certain special cases. What about general wavetypes, ones that possess no special particle-motion orientation? In this case the particle motions lie at least partially in the plane of stretching, and so the linearly transformed wave equation nonphysically specifies nonorthogonal particle-motion directions. The stretched wave is therefore only kinematically correct. This does not mean that the stretching operation is not useful. After all, geophysicists normally assume hyperbolic moveout on all events, even though it is not strictly true. In practice it is usually a good approximation for reasonable offsets. Assuming a hyperbolic moveout is the same thing as assuming an elliptical wavefield, so this simple stretch model applies in any case where the standard hyperbolic approximation can be used.

2.2   Plane solutions

In section 2.1 I did not delve into the physics of elliptical anisotropy, although as we saw it can be derived on a physical basis by examining SH waves propagating in a symmetry plane. For more complicated kinds of anisotropy there is no simple trick like "stretching isotropy" to greatly simplify things, and we are forced to fall back on the fundamentals of the problem.

Solving the anisotropic elastic wave equation analytically is a challenge, one it is better to avoid if possible. Is there a simpler way to proceed? When a wave intersects a receiver array we usually approximate it as a plane wave, even though we know the wavefront is not infinite and planar but in reality is a small part of a curved wavefront. Similarly, we can perform a plane-wave decomposition on the elastic wave equation by Fourier transformation, which converts the difficult differential equation into a tractable eigenvalue-eigenvector matrix-algebra problem (the Christoffel equation).

We can consider this plane-wave representation as an alternate, simpler domain in which to study anisotropy. The obvious question is how to relate anisotropic properties as expressed in the $(k_x, k_z; \omega)$ domain back to the physical $(x, z; t)$ domain. While it can be done by Fourier-transformation, for our purposes it is better to look for simple geometrical constructions. There is a natural way to do this, by considering graphs of energy (group) velocity versus direction and plane-wave (phase) slowness (inverse velocity) versus direction.

The group-velocity graphs show where the energy is going, and so can be considered as a sort of "cartoon" of the impulse response of the medium. Section 2.4.1 shows several examples of just how good an approximation to the full-waveform impulse response a simple group-velocity graph is. To emphasize this similarity, throughout the thesis I will refer to group-velocity graphs as "impulse-response surfaces".

The phase-slowness graphs, also called dispersion relations[3] or simply "slowness surfaces", have no obvious physical significance but are a convenient theoretical tool. In Appendix B I discuss the geometrical relationships tying these constructions together in detail, and derive the mathematical formulas underlying many of the figures in Chapters 2 and 3. These relationships between phase velocity, group velocity, and dispersion relations are considered fundamental in anisotropy; I will treat them as assumed background knowledge for the remainder of this thesis.

---

[3] Note I am calling a graph of k_z/ω versus k_x/ω a dispersion relation. All of the examples in this thesis are nondispersive, meaning the dispersion relation is independent of ω. Beware: the term "dispersion relation" is often also used (especially in other fields) to mean a graph of ω versus k. I will *not* use the term in this way.

2.3 Transverse isotropy

The simplest physically realizable anisotropic symmetry system is axisymmetric anisotropy, also called transverse isotropy or just "TI" for short. Axisymmetry implies that the properties of the medium in a given direction depend only on the angle between that direction and the symmetry axis direction. The symmetry direction is usually associated with some dominant global directed influence such as gravity or regional stress. If gravity, then the symmetry direction should be vertical, and we get "TIV" (Transverse Isotropy with a Vertical axis). If regional stress, then the symmetry direction should be horizontal, and we get "TIH" (Transverse Isotropy with a Horizontal axis) (Winterstein, 1990).

2.3.1 Mathematics of transverse isotropy

The Christoffel equation is simply the elastic wave equation Fourier transformed over space and time. It specifies the propagation velocity and particle-motion direction for each plane-wave component in the Fourier domain, and takes the form of an eigenvalue-eigenvector problem:

$$\underset{\sim}{D}\,\underset{\sim}{C}\,\underset{\sim}{D}^{T}\,\mathbf{v}_n = -\rho\Big(\frac{\omega_n}{k}\Big)^{2}\,\mathbf{v}_n \quad ;$$

(2.4)

$$\underset{\sim}{D} = \frac{1}{k}\begin{bmatrix} k_x & 0 & 0 & 0 & k_z & k_y \\ 0 & k_y & 0 & k_z & 0 & k_x \\ 0 & 0 & k_z & k_y & k_x & 0 \end{bmatrix} \quad .$$

In this equation ρ and the 6 by 6 symmetric matrix $\underset{\sim}{C}$ define the homogeneous medium; ρ gives the density and the stiffness matrix $\underset{\sim}{C}$ gives the elastic constants. (See Appendix A for more details about the $\underset{\sim}{C}$ matrix in TI media.) The 3 by 6 derivative matrix $\underset{\sim}{D}$ defines the plane-wave propagation direction under consideration. $\underset{\sim}{D}$ is a function of the wavenumber vector (k_x, k_y, k_z). The leading $1/k$ normalizes the wavenumber vector ($k = |\mathbf{k}| = |(k_x, k_y, k_z)| = \sqrt{k_x^2 + k_y^2 + k_z^2}$). Finally, ω_n and $\mathbf{v}_n$ define the resulting three wave modes; for each n, $\mathbf{v}_n$ is the particle-motion direction, and (ω_n/k) is the associated phase velocity.

This equation seems pretty straightforward, and in some ways it is. For any wavenumber vector **k**, the symmetry of the matrix $\underset{\sim}{\mathbf{D}}\,\underset{\sim}{\mathbf{C}}\,\underset{\sim}{\mathbf{D}}^T$ assures that the underlying eigenvalue-eigenvector problem will be well behaved; we can always find three distinct modes associated with three orthogonal particle-motion directions. Solving equation (2.4) for individual **k** is not the problem; things get interesting later on when we start trying to create continuous *global* solutions defined for all **k** in three dimensions at the same time. For the moment we will proceed in ignorance with the simpler case of two-dimensional transverse isotropy, and assume that things will work. As it turns out, in the two-dimensional case they will.

Now that we have been properly warned, let us proceed directly to the simplified problem by requiring axisymmetry about the z axis; then equation (2.4) multiplied out becomes:

$$
\begin{bmatrix}
C_{11}k_x^2 + C_{66}k_y^2 + C_{55}k_z^2 & (C_{11} - C_{66})k_x k_y & (C_{13} + C_{55})k_x k_z \\
(C_{11} - C_{66})k_x k_y & C_{66}k_x^2 + C_{11}k_y^2 + C_{55}k_z^2 & (C_{13} + C_{55})k_y k_z \\
(C_{13} + C_{55})k_x k_z & (C_{13} + C_{55})k_y k_z & C_{55}k_x^2 + C_{55}k_y^2 + C_{33}k_z^2
\end{bmatrix}
\begin{bmatrix} v_x \\ v_y \\ v_z \end{bmatrix}
$$

$$
= \rho\omega^2 \begin{bmatrix} v_x \\ v_y \\ v_z \end{bmatrix} .
$$

(2.5)

Axisymmetry about the z axis implies that the x and y axes are equivalent. Since it is redundant to use both spatial coordinates, we will arbitrarily set $k_y = 0$, thus confining ourselves to the 2-dimensional cross section in the x-z plane. (I also preferentially use the x and z elastic constants; for example I will use $C_{55} = C_{xzxz}$ instead of $C_{44} = C_{yzyz}$, etc.)

Since we are dealing with non-dispersive media, only the direction of the plane wave determines its velocity, not its wavelength. This can be incorporated into the notation by letting $k_x = k\sqrt{s}$ and $k_z = k\sqrt{c}$, where s is the square of the sine of the angle between the symmetry axis and the direction of propagation of the plane wave, and $c = 1 - s$ is the square of the cosine. (In the notation of Appendix B, $s = \sin^2 \phi_w$, $c = \cos^2 \phi_w$.)

Unfortunately, this change of variables loses the sign of k_x and k_z. However, examining the Christoffel equation we see that changing the sign of k_x merely changes the sign of v_x, and that changing the sign of k_z merely changes the sign of v_z. Since the z-y and x-y planes are mirror planes we can assume k_x and k_z are both positive without loss of

generality. We'll just have to be a little careful about any derivatives we take on the symmetry planes, since s and c are at their extrema there.

Incorporating this change in notation, the Christoffel equation becomes

$$\begin{bmatrix} C_{11}s + C_{55}c & 0 & (C_{13} + C_{55})\sqrt{sc} \\ 0 & C_{66}s + C_{55}c & 0 \\ (C_{13} + C_{55})\sqrt{sc} & 0 & C_{55}s + C_{33}c \end{bmatrix} \begin{bmatrix} v_x \\ v_y \\ v_z \end{bmatrix} = \rho(\frac{\omega}{k})^2 \begin{bmatrix} v_x \\ v_y \\ v_z \end{bmatrix}. \qquad (2.6)$$

It is convenient to use prescience and make yet another change of variables at this point. Let

$$\delta_{33} = C_{33} - C_{55},$$

$$\delta_{11} = C_{11} - C_{55}, \qquad (2.7)$$

and

$$\chi = C_{13} + C_{55}.$$

We can also identify the term ω/k in equation (2.6) as the velocity V_w of the plane wave whose direction of propagation is determined by s and c. In terms of these new variables, the Christoffel equation becomes

$$\begin{bmatrix} C_{11}s + C_{55}c & 0 & \chi\sqrt{sc} \\ 0 & C_{66}s + C_{55}c & 0 \\ \chi\sqrt{sc} & 0 & C_{55}s + C_{33}c \end{bmatrix} \begin{bmatrix} v_x \\ v_y \\ v_z \end{bmatrix} = \rho V_w^2 \begin{bmatrix} v_x \\ v_y \\ v_z \end{bmatrix}. \qquad (2.8)$$

(It easily fits on one line now, and several of the terms are zeroes: a big improvement.)

Solving for the wave modes

One obvious solution of equation (2.8) is found by setting v_x and $v_z = 0$. Doing this, we obtain

$$C_{66}s + C_{55}c = \rho V_w{}^2 \quad \text{and} \quad \begin{bmatrix} v_x \\ v_y \\ v_z \end{bmatrix} = \gamma \begin{bmatrix} 0 \\ 1 \\ 0 \end{bmatrix}, \tag{2.9}$$

where γ is an arbitrary constant.

This is a pure shear mode, since the direction of propagation (chosen to lie in the x-z plane) is always perpendicular to that of the particle-motion direction (y). Such a propagation mode is called an SH wave. Note that the phase-slowness curve for this wave type is always elliptic.[4] For the reasons given in sections B.3 and 2.1.1, this implies that the impulse-response surface for this mode is also always elliptical. No matter how anisotropic the media may be, SH waves will always have hyperbolic move out.

Since any two different eigensolutions are guaranteed orthogonal (see Appendix A), the other two solutions of equation (2.8) must have $v_y = 0$. Substituting this in, we remove the solution we have already found and equation (2.8) reduces to

$$\begin{bmatrix} C_{11}s + C_{55}c & \chi\sqrt{sc} \\ \chi\sqrt{sc} & C_{55}s + C_{33}c \end{bmatrix} \begin{bmatrix} v_x \\ v_z \end{bmatrix} = \rho V_w{}^2 \begin{bmatrix} v_x \\ v_z \end{bmatrix}. \tag{2.10}$$

The solution of equation (2.10) is:

$$\tfrac{1}{2}\left(C_{55} + C_{33}c + C_{11}s + m\sqrt{(\delta_{33}c - \delta_{11}s)^2 + 4sc\chi^2} \right) = \rho V_w{}^2$$

and

$$\begin{bmatrix} v_x \\ v_y \\ v_z \end{bmatrix} = \gamma \begin{bmatrix} 2\chi\sqrt{sc} \\ 0 \\ m\sqrt{(\delta_{33}c - \delta_{11}s)^2 + 4sc\chi^2} + \delta_{33}c - \delta_{11}s \end{bmatrix}, \tag{2.11}$$

where m is either plus or minus one and γ is once again an arbitrary constant.

The sign of m selects one of the two remaining propagation modes. Although perhaps not obvious from equation (2.11), the particle-motion directions for these two propagation

---

[4]The "stretching would break particle-motion orthogonality" argument we used in section 2.1.2 is still valid: the other two modes cannot be stretched.

modes are indeed always perpendicular to each other.[5]

One important thing to notice is that the phase velocity for the $m = 1$ solution is always greater than that for the $m = -1$ solution for any s. Our isotropic intuition would suggest that the $m = 1$ solution must be approximately a P wave and the $m = -1$ solution approximately an SV wave. As we show in the next section, this is only true for materials reasonably close to being isotropic. To avoid bias, we will instead refer to the two solutions as the "fast" and the "slow" wave solutions. This concept will prove even more useful later in section 3.3.4.

Is TI two or three dimensional?

In the previous section we were able to split the transversely isotropic Christoffel equation into two decoupled systems, whose solutions are given by equations (2.9) and (2.11). The SH solution corresponds to the case of elliptical anisotropy already discussed in section 2.1. The other two solutions conveniently form a complete system of two-dimensional anisotropy, with two wavetypes and two dimensions, x and z. In the following sections we will examine this two-dimensional anisotropic system, which corresponds in three dimensions to a y line source with particle motion in the x-z plane.

2.3.2 TI kinematic behavior

In this section we examine how the kinematic properties of the two "interesting" (non-SH) wavetypes vary according to the values of four of the six parameters required to specify a transversely isotropic medium: C_{11}, C_{33}, C_{55}, and C_{13}. (From equation (2.11) we already know that C_{66} affects only the elliptical SH solution, and ρ merely functions as a global scale factor for the phase velocities.)

Impulse response versus C_{13}

Since χ only occurs multiplied by sc in equation (2.11), C_{13} has no part in determining either the vertical ($s = 0$) or horizontal ($c = 0$) velocity of either the fast or slow wave types. It controls the type of behavior in between, however, which is what makes it the

---

[5]Equation (2.11) has another interesting symmetry as well. The kinematics are left unchanged if we swap s and c, and C_{33} and C_{11}; the particle-motion direction is left unchanged if we also change the signs of m and v_z. This symmetry comes in handy when calculating paraxial approximations (Muir, Dellinger, and Karrenbach, in preparation).

most interesting elastic constant.[6] We begin by showing that for a particular "central" value of $|\chi|$ the fast and slow solutions display elliptical anisotropy.

Elliptic Constraint

For the phase-slowness surface and thus the impulse-response surface to be an ellipse, $V_w{}^2$ must be a linear function of s. From equation (2.11) we see that this can only occur when the quantity under the radical

$$\sqrt{(\delta_{33}c - \delta_{11}s)^2 + 4sc\chi^2} = \sqrt{(\delta_{33}c)^2 + 2sc(2\chi^2 - \delta_{33}\delta_{11}) + (\delta_{11}s)^2} \qquad (2.12)$$

is the square of a linear term that maintains the same sign over the interval 0 to 1. This occurs when either

$$\chi = 0 \quad \text{(if } \delta_{33}\delta_{11} < 0) \qquad \text{or} \qquad \chi = \pm\sqrt{\delta_{33}\delta_{11}} \quad \text{(if } \delta_{33}\delta_{11} > 0). \qquad (2.13)$$

If δ_{33} and δ_{11} are both negative, there are no solutions of equation (2.13) that are not prohibited by the energy constraints. This is easy to prove by showing that the minimal allowed value of χ^2 is too large. However, if C_{66} is small, C_{11} and C_{33} are near in value, and C_{13} is as negative as allowed, ellipticity can still almost be reached (Helbig and Schoenberg, 1987). (See Figure 2.10 for an example.)

If equation (2.13) is satisfied, both the fast and slow solutions will have an elliptical impulse-response surface and slowness surface. If δ_{33} and δ_{11} are both positive (the usual case), the slow solution is in fact exactly circular (but not isotropic, because that would require the particle motion to be that of a pure SV mode, which it normally isn't). The top plot in Figure 2.7 and the middle plot in Figure 2.10 show finite-difference examples for the two cases in equation (2.13).

Note also the bottom plot in Figure 2.7, which shows how the $\chi = 0$ case manages to result in two ellipses even if δ_{33} and δ_{11} have the same sign: the two ellipses intersect. The trick is that each ellipse is a chimera consisting of pieces of both the fast and slow wavetypes. If χ is perturbed, the two ellipses immediately break into their component parts and the phantom triplications connecting the erstwhile ellipses appear. (As we will see in section 3.5.1, this sort of behavior is much more common than one might think.)

---

[6]That is why I have chosen the symbol "χ" for this term — its arms point in the 45° directions, suggesting the propagation directions this constant most affects.

Types of behavior

The square root term in equation (2.11) causes deviation from an ellipse. It is this deviation which creates the "interesting" behaviors of the phase-slowness curve. Under the square root is the sum of two terms,

$$4sc\chi^2 \tag{2.14}$$

and

$$(\delta_{33}c - \delta_{11}s)^2, \tag{2.15}$$

each of which is usually positive but can just touch zero. The term in equation (2.14) is zero for $s = 0$ and $s = 1$ and maximal halfway in between. The term in equation (2.15) is maximal at $s = 0$ and $s = 1$, and if δ_{33} and δ_{11} have the same sign, it passes through zero at

$$s_t = \frac{\delta_{33}}{\delta_{33} + \delta_{11}}. \tag{2.16}$$

The magnitude of χ determines the relative weight of the two terms. If χ is small, the term in equation (2.15) dominates. This causes the phase-slowness curve to bulge in for the slow solution and out for the fast solution at $s = s_t$. If δ_{33} and δ_{11} do not have the same sign, this term never passes through zero and so there is no resulting bulge. If χ is large, the term in equation (2.14) dominates. This causes the phase slowness to bulge in for the slow solution and out for the fast solution at $s = 0$ and $s = 1$.

This behavior is demonstrated in Figure 2.4. The plot consists of two sections. The upper set of plots numbered 1 through 10 are slowness surfaces (dispersion relations); the lower set numbered 1' through 10' are the corresponding impulse-response surfaces (group-velocity surfaces). The thin line is for the fast solution; the fatter line is for the slow solution. All plots are to the same scale. χ increases throughout the sequence of plots.

Several of the values of χ were chosen for their special properties. These are:

1. $\chi = 0$. In a sense this is the "minimal" value of χ, because only χ^2 occurs in equation (2.11). For this value the slowness surface consists of two interlocking ellipses, with the slow solution traversing the outer parts and the fast solution the inner (Helbig and Schoenberg, 1987). Note that the vertical ellipse of the slowness surface corresponds
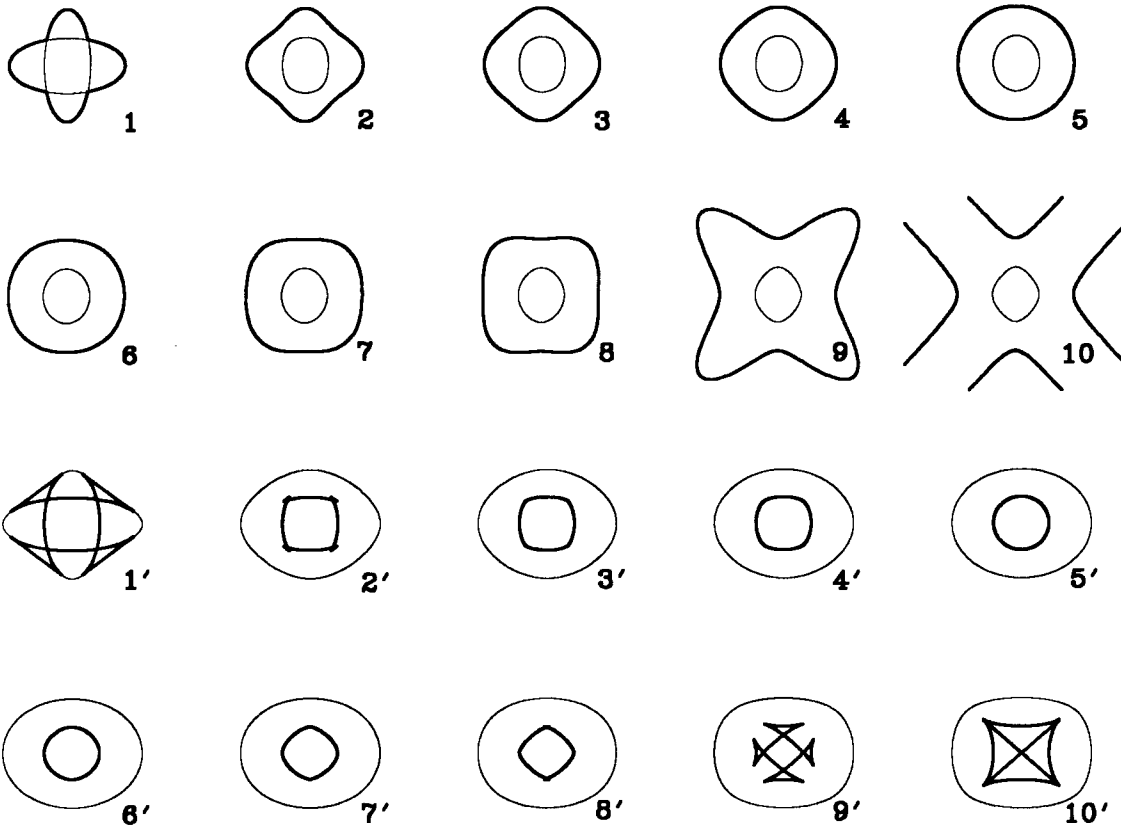
FIG. 2.4. Behavior of the slowness surface (upper set) and impulse-response surface (lower set) as C_{13} increases. The thick line is the slow solution and the thin line is the fast solution. (Slowness surface number 10 is clipped since the "arms" of the plot extend off to infinity.)

with the horizontal one of the impulse-response surface, and vice–versa. In the direction s_t, the fast and slow solutions just touch. Unless C_{11} or C_{33} equal C_{55}, this is the only case in which the two solutions can do so.

2. "Reality." These cases were all calculated using the elastic constants of the "Green-horn shale" (Jones and Wang, 1981), but allowing C_{13} to vary. This case is plotted using the real value of C_{13}. Note that the slow solution triplicates for this rock.

3. Here the slowness surface of the slow solution is on the borderline between being concave and convex. As is shown in Appendix B, points of concavity of the slowness surface are associated with points of triplications of the impulse-response surface. "Borderline" triplications such as this turn out to occur at angles where one of the two terms under the radical in equation (2.11) is zero. In this case it is the term given in equation (2.15), and

the incipient triplication is in the phase direction $s = s_t$.

5. For this plot the elliptic constraint is satisfied. Both the slowness surface and impulse-response surface are exactly circular for the slow solution and elliptical for the fast.

7. and 8. Here we are again at borderline triplications of the slow solution, at the top for plot 7 and at the sides for plot 8. This time it is the term given in equation (2.14) that is zero at the triplications. Whether triplications first occur at the top or side depends on the relative sizes of C_{11} and C_{33}.

9. and 10. Plot 9 just violates energy constraints, and so is physically nonrealizable. (See equation (A.14) on page 151 for more details.) That is a bit of a sham, though; the energy constraint being violated is

$$C_{13}^2 < C_{33}(C_{11} - C_{66}), \tag{2.17}$$

which depends on C_{66} — but C_{66} only affects the behavior of the SH wave, which is not being considered in this section. Plot 10 just violates a weaker constraint, that the phase velocities must be positive for all s. For transverse isotropy this constraint requires that $C_{13} \leq \sqrt{C_{11}C_{33}}$. This is equivalent to setting C_{66} to 0, the minimal physically allowable value, in equation (2.17).

Note that while the character of the slow solution changes dramatically, the fast solution changes only slowly, and with no major changes in behavior. If we had continued to increase χ, the fast solution would have eventually also started to triplicate at $s = s_t$. However, this value of χ is far outside the bounds of the energy constraint. This is always the case, as can be shown in several ways. (We will do it mathematically in the subsection starting on page 26; Helbig (in preparation) gives a very good general proof based on purely geometrical arguments.)

Figure 2.4 showed the normal case where δ_{11} and δ_{33} are both positive. If δ_{11} and δ_{33} are not of the same sign, the behavior is similar but the two ellipses are nested instead of interlocking. (This is the other solution to equation (2.13).) Figure 2.5 shows how the transition occurs. χ is held at zero in all the plots. δ_{33} and δ_{11} start out positive and equal in plot 1; δ_{33} is lowered in steps until it reaches zero in plot 4 and finally becomes negative in plot 5. All plots are to the same scale. (Believe it or not, none violate energy constraints.)
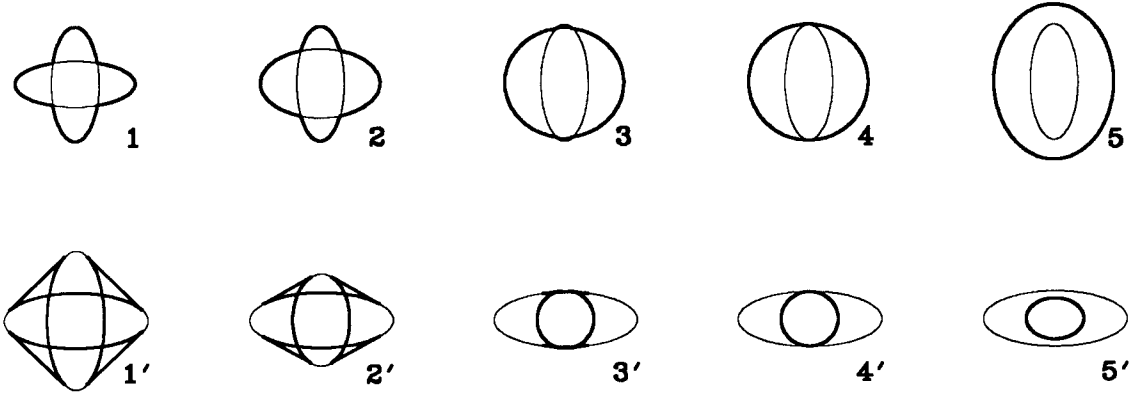
FIG. 2.5. Behavior of the slowness surface (upper set) and impulse-response surface (lower set) as C_{33} decreases. The dark line is the slow solution and the light line is the fast solution.

Triplications

It is difficult to migrate in the time domain if there are triplications, since energy can travel in the same direction with more than one velocity. Thus it is important to know for what ranges of elastic constants triplications do not occur.

From the previous discussion, we have a good idea as to the general shape of the slowness surface as a function of χ. We thus know to look for at most three different s for which borderline triplications can occur, and we know beforehand whether the values of χ at each of these are upper or lower bounds. It is difficult but straightforward to derive analytical formulas that give the exact bounds. The results will be presented here.

The top and side case

A borderline triplication occurs when $d\phi_r/d\phi_w$ and $d^2\phi_r/d\phi_w^2$ are simultaneously zero. For $s = 0$ and $s = 1$ the second derivative is always zero because of symmetry. Thus we need only solve for when the first derivative is zero. Using equation (B.4) from section B.4 this is not too difficult.

For $s = 0$, the result is that the fast solution can only triplicate if χ^2 is negative – which means never. The slow solution triplicates when

$$\chi^2 > \begin{cases} +C_{11}\delta_{33}, & \text{if } \delta_{33} > 0; \\ -C_{55}\delta_{33}, & \text{if } \delta_{33} < 0. \end{cases} \tag{2.18}$$

For $s = 1$ the result is the same, except that we must replace δ_{33} with δ_{11} and C_{11} with C_{33}.

The off-axis case

It is not obvious where to look for the borderline off-axis triplications. Since the on-axis triplications occurred where one of the two guaranteed-nonnegative terms under the square root in equation (2.11) becomes zero, we might be tempted to try looking where the other term is zero, in the direction $s = s_t$. It is hopeless to evaluate $d^2\phi_r/d\phi_w^2$. I was only able to solve the problem by guessing that $s = s_t$ might be the required angle and verifying that indeed this was the case.

I started by rewriting equation (B.4) in the form of a formula whose sign indicates whether a triplication is occurring or not. This was evaluated at $s = s_t$, and after a great deal of algebra (being careful not to introduce unaccounted-for spurious roots) was simplified to a third-degree polynomial in $|\chi|$. The derivative of the formula with respect to s was also computed and evaluated at $s = s_t$. This resulted after yet more algebra in a fourth-degree polynomial, which was found to have as a factor the third-degree polynomial already derived. Thus as a function of s our original formula had only double roots at $s = s_t$, and so this was indeed the value of s at which borderline triplications occur.

Having thus proven my guess correct, the equation to solve is

$$|\chi|^3 + A|\chi| + B = 0,$$

where

$$A = -\left(3C_{55}{}^2 - C_{55}(C_{33} + C_{11}) + 3C_{11}C_{33}\right) \qquad (2.19)$$

and

$$B = -2m|C_{11}C_{33} - C_{55}{}^2|\sqrt{\delta_{33}\delta_{11}}.$$

The solution to this polynomial is always of the form

$$|\chi| = 2m\sqrt{-\frac{A}{3}}\cos(\frac{\phi+2\pi K}{3}),$$

where

$$\cos\phi = \sqrt{\frac{B^2}{4}\bigg/\frac{-A^3}{27}} \qquad (2.20)$$

and

$$K = 0, 1, 2.$$

The $K = 0$ solution for $m = -1$ and the $K = 1, 2$ solutions for $m = 1$ are spurious, since $|\chi| \geq 0$ and these solutions are always negative. We know from the example beginning on page 23 that after the slow solution begins to triplicate at $s = s_t$, it continues to triplicate for higher values of $|\chi|$ until the energy constraints are violated. Thus the smaller of the two positive solutions of equation (2.20) for $m = -1$ must be the solution we want. This is always the $K = 2$ solution. The $K = 1$ solution must therefore always violate the energy constraints. For $m = 1$, only the $K = 0$ solution is not spurious. This solution is always larger than the $K = 1$ solution for $m = -1$, and thus the fast solution cannot triplicate in any direction for any physically allowed set of elastic constants. These results confirm those of Lyakhovitskiy (1984).

2.3.3   TI particle-motion behavior

As we have already seen, one wave propagation mode is an SH wave. Particle motion in this mode is perpendicular to both the z axis and to the direction of propagation. In the rest of this section we will be concerned with the other two transversely isotropic solutions.

The particle-motion directions are given by equation (2.11), but in an inconvenient form. It is better to write the formula in terms of the angle between the direction of plane-wave propagation and the direction of particle motion. Let us call this angle ϕ_a,

and let a be the square of the sine of this angle. Then (after a great deal of algebra):

$$a = m\frac{\left((2s-1)t_1 - t_2\right)\sqrt{t_1^2 - t_2\chi}}{2(t_2\chi - t_1^2)} + \frac{1}{2},$$

where

$$t_1 = s(\delta_{33} + \delta_{11}) - \delta_{33}$$

and

$$t_2 = 4s(s-1)\chi.$$

(2.21)

Note that since the eigensolutions are perpendicular, $a|_{m=1} + a|_{m=-1} = 1$.

Pure modes

Solving equation (2.21) to find when a is 0 or 1 yields conditions for the existence of pure P and SV modes, respectively. The result is that pure P and SV modes occur for 3 values of s:

$$s = 0, \qquad s = 1, \qquad \text{and} \qquad s = \frac{(\delta_{33} - \chi)}{(\delta_{33} - \chi) + (\delta_{11} - \chi)}.$$

(2.22)

(This agrees with Sakadi (1941).)

We shall consider the case $s = 0$ first. This corresponds to a plane wave traveling along the axis of symmetry. As shown by Auld (1973), waves traveling down a symmetry axis must always be pure modes. This is indeed the case we find here. There are two solutions, a pure P mode with velocity $\sqrt{C_{33}/\rho}$, and a pure SV mode with velocity $\sqrt{C_{55}/\rho}$. There is an interesting complication here, though. The fast solution given when $m = 1$ is the P one only if $\delta_{33} > 0$ (that is, if $C_{33} > C_{55}$). If $\delta_{33} < 0$, the fast solution is in fact the SV one.

The case for $s = 1$ is very similar. Again we find that there are two pure modes, a P one with velocity $\sqrt{C_{11}/\rho}$, and an SV one with velocity $\sqrt{C_{55}/\rho}$. The fast solution can again be either the P or SV mode, whichever is faster.

The third pure-mode direction given in equation (2.22) does not lie on any symmetry axis. It only exists if $\delta_{33} - \chi$ and $\delta_{11} - \chi$ have the same sign. For this pure-mode direction, if χ is positive the fast solution is the P one and the slow solution is the SV one. If χ is
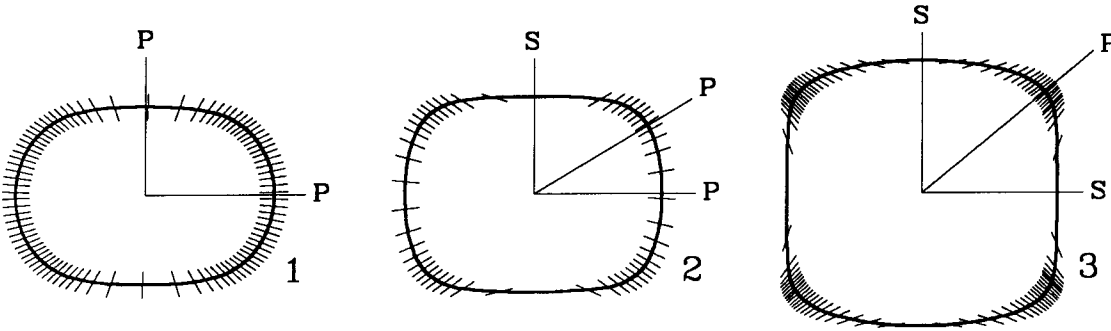
FIG. 2.6. The particle motion and impulse-response surface of the fast solution for three different values of C_{55}, with C_{55} increasing to the right. The lines indicate the directions in which pure modes exist, and the "hairs" show the direction of particle motion.

negative, it is the other way around.

Anomalous particle motion

From what we have concluded so far it is clear that if any of δ_{33}, δ_{11}, or χ is negative the particle motion must exhibit some very strange behavior. If exactly one of δ_{33} and δ_{11} is negative, for example, the same solution that is a P wave at $s = 0$ is an SV wave at $s = 1$, and vice–versa. If δ_{33} and δ_{11} are of the same sign but χ is not, then the solution that is a P wave at both $s = 0$ and $s = 1$ is a pure SV wave somewhere in between! It is for such reasons that we cannot reliably call the fast solution "Quasi-P" and the slow solution "Quasi-SV", as is usually done in the literature.

Energy constraints do not permit δ_{33}, δ_{11}, and χ to all be negative at the same time. This has the result that although the fast solution does not necessarily have to be close to a P wave for every angle, it does always have to be a pure P wave for *some* angle.

The three different sorts of particle-motion behavior possible are shown in Figure 2.6. All three show the impulse-response surface for the fast solution, to the same scale. C_{55} is the only elastic constant that varies between them. χ is positive for all three. None violate energy constraints. From left to right, the cases are: 1. both δ_{33} and δ_{11} positive, 2. δ_{33} negative and δ_{11} positive, and 3. both δ_{33} and δ_{11} negative. Also possible, but not shown, is the case where δ_{33} is positive and δ_{11} is negative. In this case the particle motion is approximately vertical all the way around. Allowing χ to be negative does not add any new types of behavior.

Putting the sign back in the sine

Equation 2.21 is concise and in a convenient form, but is not useful computationally because it only gives the square of the sine of the angle of interest, ϕ_a. We will measure ϕ_a as positive in the same direction that ϕ_w is positive. As always, we assume that ϕ_w is between $0°$ and $90°$.

Let s_3 be the third pure-mode direction of equation (2.22). We will assume that χ is positive, and refer to the angle for the fast solution. Then, if $\delta_{11} > \chi$ and $\delta_{33} > \chi$, ϕ_a goes from negative to positive as s goes from 0 to 1, with ϕ_a changing sign at $s = s_3$. If $\delta_{11} < \chi$ and $\delta_{33} < \chi$, ϕ_a instead goes from positive to negative, again changing sign at $s = s_3$. If $\delta_{11} > \chi$ and $\delta_{33} < \chi$, ϕ_a is always positive; if $\delta_{11} < \chi$ and $\delta_{33} > \chi$, ϕ_a is always negative. If χ is negative these same rules apply but we must reverse the given sign of ϕ_a and refer to the angle for the slow solution instead.

2.4 Some TI finite-difference model examples

In this section I use elastic finite-difference-modeled wavefields to illustrate the points made in the earlier parts of this chapter. I proceed in three steps, working from the most theoretical to the more realistic.

2.4.1 Canonical examples

I begin by demonstrating some of the more interesting theoretical properties of transverse isotropy using examples drawn from the previous section.

The effect of C_{13}

Figure 2.7 shows 3 examples from Figure 2.4; the dotted lines overlay the corresponding plots from Figure 2.4. This suite of models shows how the impulse response varies as C_{13} decreases; all the other elastic constants are held fixed. In the top plot the "elliptical constraint" value of C_{13} was used. The qSV wavefront is exactly circular, and the qP wavefront is elliptical. The middle plot shows "Greenhorn Shale" (Jones and Wang, 1981). Note how qSV energy extends off the ends of the cusps. (These "tails" in fact reach all the way out to merge with the qP arrival, as you can see by looking ahead to Figure 2.24.) The bottom plot shows what happens if C_{13} is decreased to the "symmetry" value. The

5: Elliptic Constraint   5: Elliptic Constraint

2: Greenhorn Shale   2: Greenhorn Shale

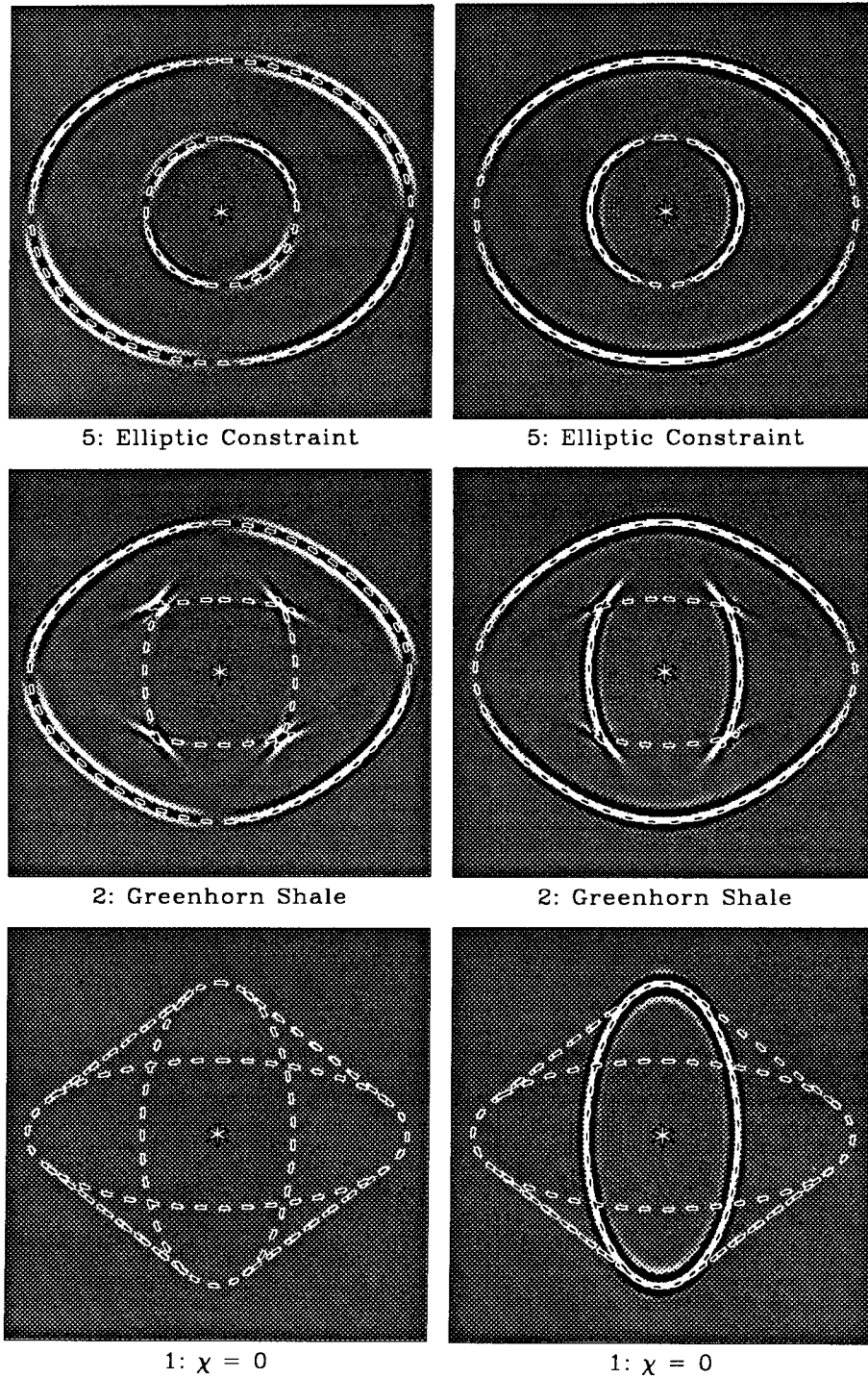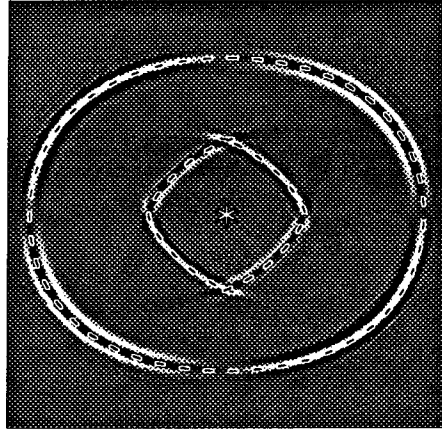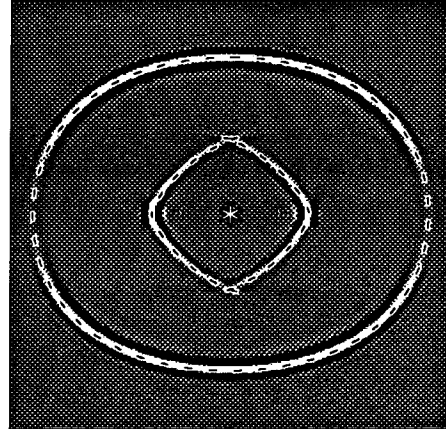1: $\chi = 0$ 1: $\chi = 0$

FIG. 2.7. Finite-difference model results corresponding to cases 5, 2, and 1 in Figure 2.4. The source is a z point force located at the center. The left column shows the x-component, the right column shows the z-component. The dotted lines show how the curves in Figure 2.4 compare with the corresponding finite-difference wavefields.
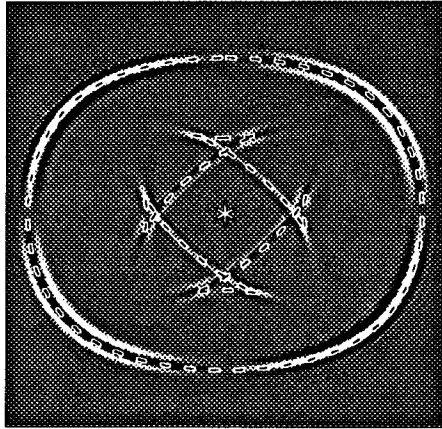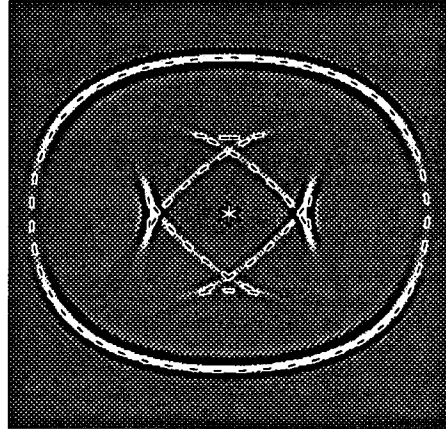
7: Borderline triplication

7: Borderline triplication

9: Energy constraint

9: Energy constraint
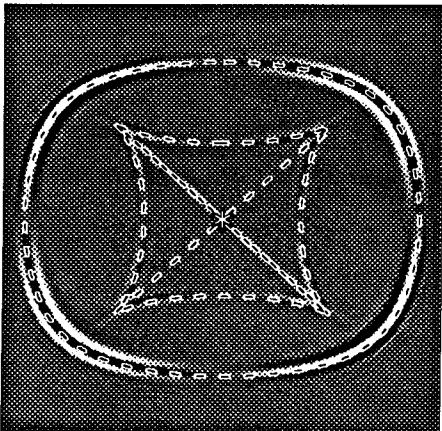
10: qSV blows up
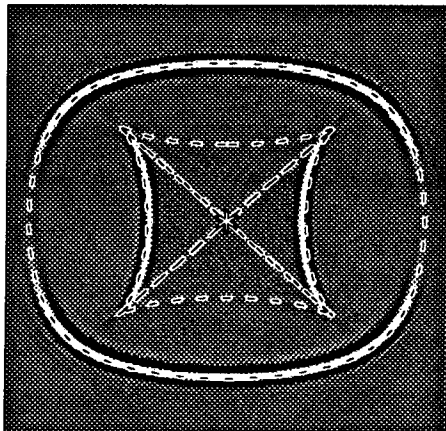
10: qSV blows up

FIG. 2.8. Finite-difference model results corresponding to cases 8, 9, and 10 in Figure 2.4. The source is a z point force located at the center. The left column shows the x-component, the right column shows the z-component. The dotted lines show how the curves in Figure 2.4 compare with the corresponding finite-difference wavefields.

qSV cusps merge with the qP wavefront and cancel parts of it out, leaving two interlocking ellipses with pure x and z particle motion. The z source used here excites only the z-sensitive ellipse, so the left plot is blank.

Figure 2.8 shows 3 more examples from Figure 2.4. This suite of models shows how the impulse response varies as C_{13} increases from the elliptic value. Again, all the other elastic constants are held fixed. In the top plot the qSV wave is just beginning to triplicate at the left and right, producing a strong amplitude anomaly. In the middle plot C_{13} has been lowered to the "physically realizable" constraint. This limit depends on the values of C_{11}, C_{33}, and C_{66}. Since C_{66} only effects the behavior of the SH mode (not shown), we shouldn't be too surprised that there is no way to tell just by looking that this wavefield is almost physically impossible. (It certainly seems less bizarre than the lower plot in Figure 2.7, which is well within the energy constraint limits.) The lowermost plot in Figure 2.8 is at a less strict but more obvious limit; for this example the qSV phase velocity reaches zero in some directions. (It is rather surprising that the finite-difference modeling program was able to step this wavefield along in time without exploding.)

Anomalous polarizations

Figure 2.9 shows the 3 examples from Figure 2.6. In this suite of models C_{55} is varied while all the other elastic constants are held fixed. The top plot is "normally" polarized, meaning there are identifiable qP and qSV wavetypes. The middle and bottom plots are anomalously polarized; the qP and qSV modes have become "mixed up". The interesting point here is to see how the transition happens. As C_{55} increases the inner qSV wavefront moves out and combines with the outer qP wavefront; the outer wavefront then moves away carrying the original qSV particle-motion direction with it.

The examples in Figure 2.9 hardly seem physically likely, but in fact many pure crystals support wavetypes that are at least as bizarre to look at. Likewise, some sets of even more extreme elastic constants can produce finite-difference results that appear deceptively normal. Figure 2.10 shows three such examples. The top plot was constructed using the elastic constants of Greenhorn Shale but with the sign of χ reversed, resulting in an extremely large negative value of C_{13}. The plot looks exactly like the middle plot in Figure 2.7, but with the sign of the x-component reversed. The middle plot shows an example of the "weird" elliptic constraint, the one that occurs when $\chi = 0$ and δ_{33} and δ_{11} have opposite sign. (If we increased C_{33} in this example so that $C_{33} = C_{55}$,

1: Normal

1: Normal

2: $C_{55} > C_{33}$

2: $C_{55} > C_{33}$

3: $C_{55} > C_{33}$ and C_{11}
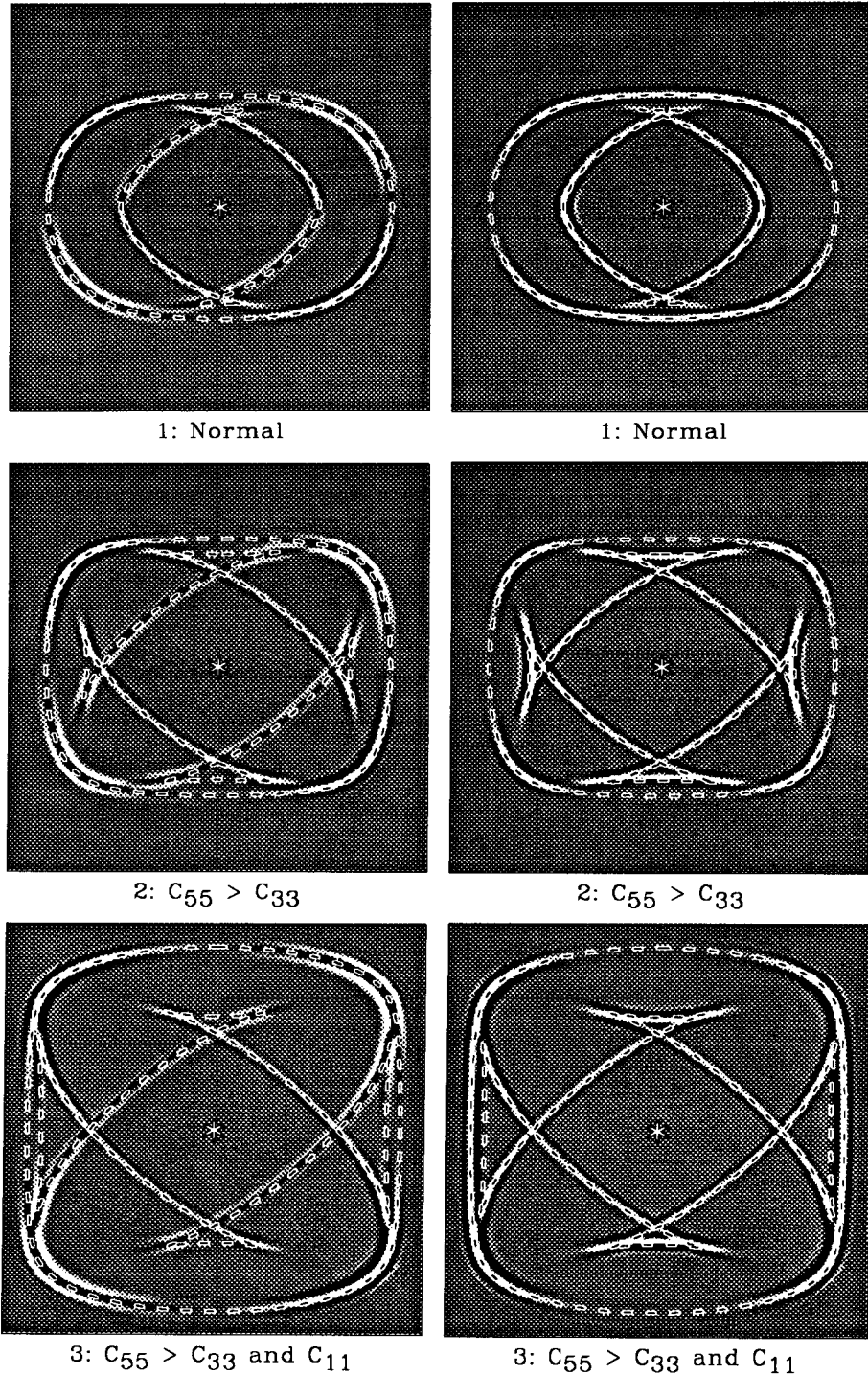
3: $C_{55} > C_{33}$ and C_{11}

FIG. 2.9. Finite-difference model results corresponding to the three cases in Figure 2.6. The source is a z point force located at the center. The left column shows the x-component, the right column shows the z-component. The dotted lines show how the corresponding curves in Figure 2.6 compare.
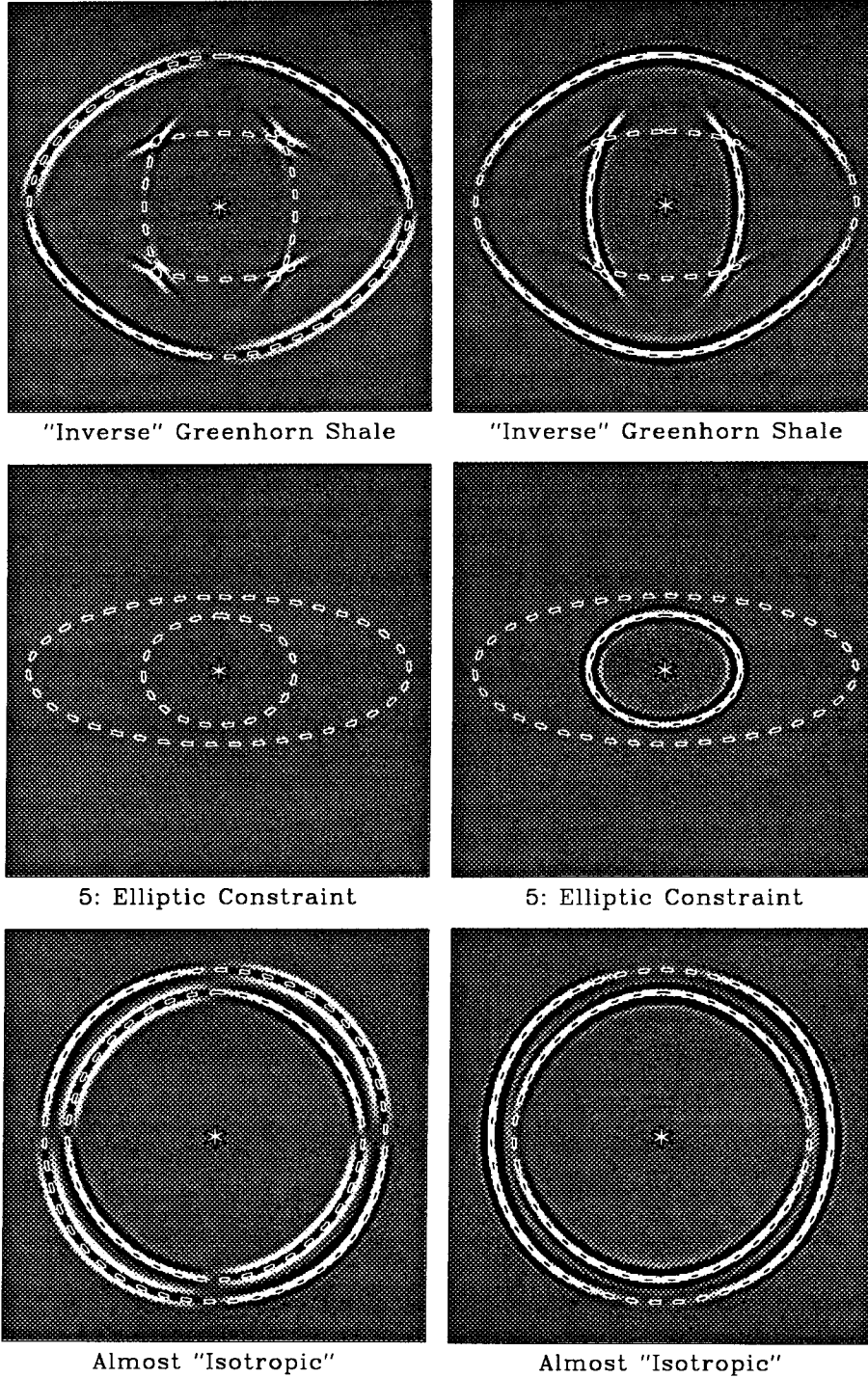
"Inverse" Greenhorn Shale   "Inverse" Greenhorn Shale

5: Elliptic Constraint   5: Elliptic Constraint

Almost "Isotropic"   Almost "Isotropic"

FIG. 2.10. Three extreme elastic models that look deceptively normal. The source is a
z point force located at the center. The left column shows the x-component, the right
column shows the z-component. The top picture shows "Greenhorn Shale" with the sign
of χ reversed. The middle picture corresponds to plot 3 in Figure 2.5. The bottom picture
is an example of a "nearly isotropic" but anomalously polarized medium. None of these
examples violate energy constraints.

as in plot 4 in Figure 2.5, we would get an "isotropic" wavefront that had a pure z particle-motion direction all the way around.) The bottom plot shows an example of a "nearly isotropic" wavefront with decidedly non-isotropic particle-motion directions (on both symmetry axes the fast wavetype is a shear wave). This possibility was pointed out by Helbig and Schoenberg (1987).

2.4.2 A laboratory core-measurement simulation[7]

The examples in the previous subsection are entertaining and informative, but are probably rather more extreme than any rocks geophysicists are likely to encounter. In this subsection I present a more geophysically relevant example, modeled after a laboratory study by Vernik and Nur (1990).

FIG. 2.11. The qP-qSV impulse-response surface for Bakken shale core sample #10931 (Vernik and Nur, 1990); the elastic constants are listed in Table C.1. The dotted lines are best-fitting 90° paraxial ellipses. The two angles show the direction of "vertical" in Figures 2.13 and 2.12.
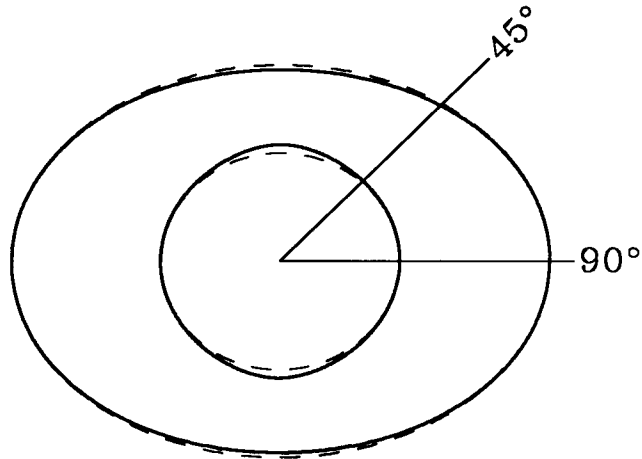
Vernik reported some difficulties when he tried to measure the elastic wave velocities in some shale samples. His original experimental setup consisted of cores of shale with transducers glued at either end. The cores were cut at angles of 0°, 90°, and 45° to the layering in the shale. Velocity measurements for the 0°-cut and 90°-cut cores proceeded without difficulty, and showed that some of the cores had P-wave velocity anisotropies ($\sqrt{C_{11}/C_{33}} - 1$) of up to 37%. The 45°-cut cores, however, produced weak or indistinct signals. Why should these cores have acted differently?

---

[7]This section is based on "Do core-sample measurements record group or phase velocity?" (Dellinger and Vernik, in preparation) .
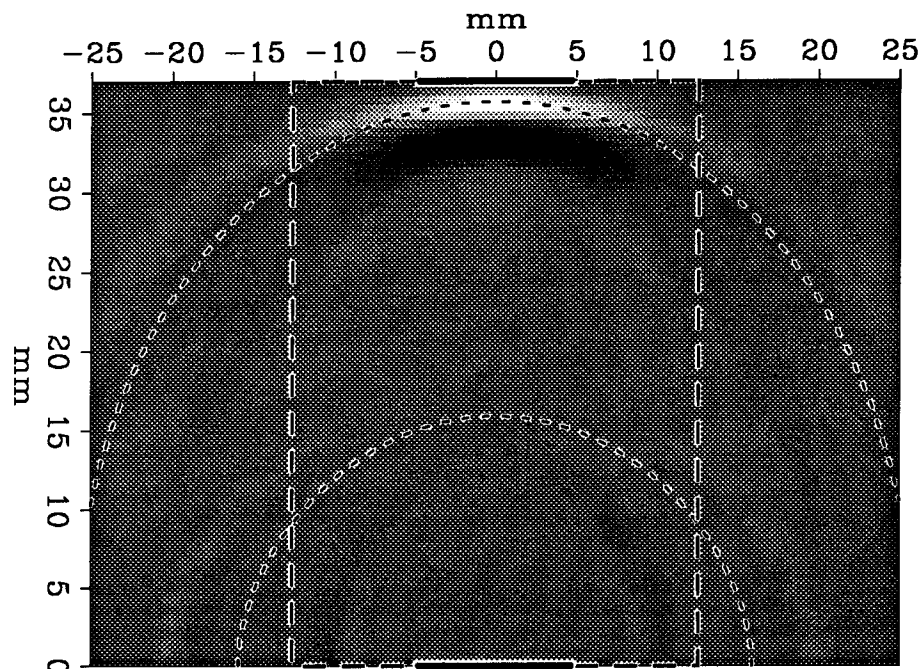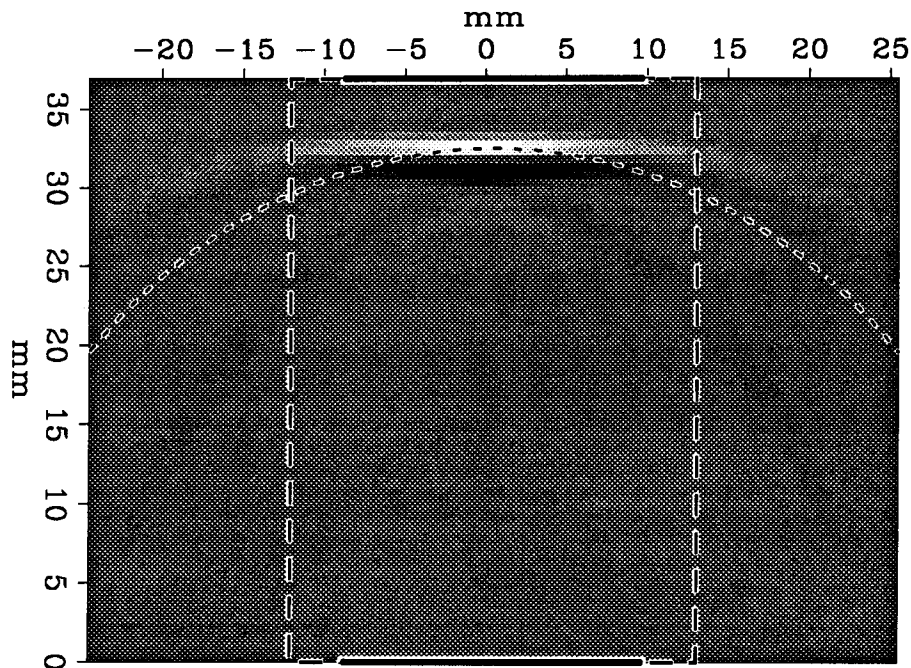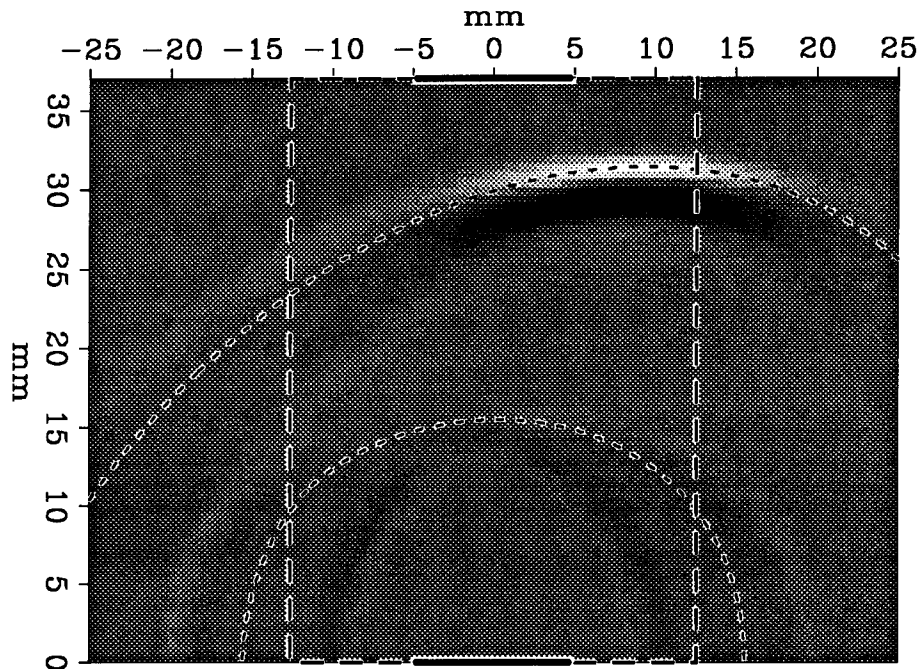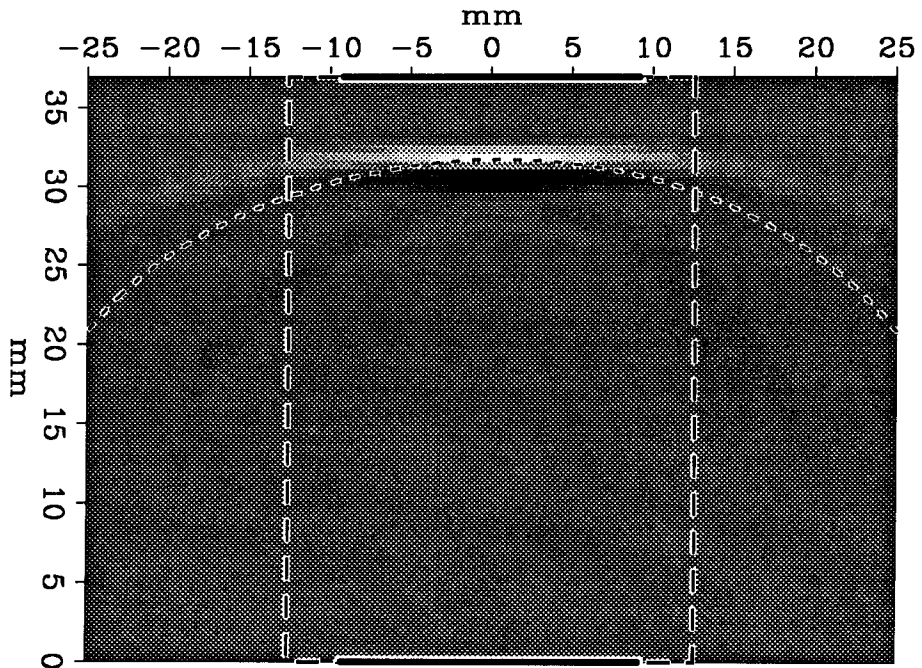
FIG. 2.12. A simulation of waves propagating in a shale core sample. The layering in the shale is oriented vertically. The outlines of the core sample are shown by the dashed line. The position and size of the source (at bottom of core) and receiver (at top) transducers are shown by the heavy black lines. The dotted line shows the theoretical impulse-response surface for a point source at the center of the source transducer. The source has a dominant frequency of .970MHz and the vertical P velocity is 4.66 km/sec. The upper snapshot is at 7.77 μsec, and the lower is at 15.93 μsec.
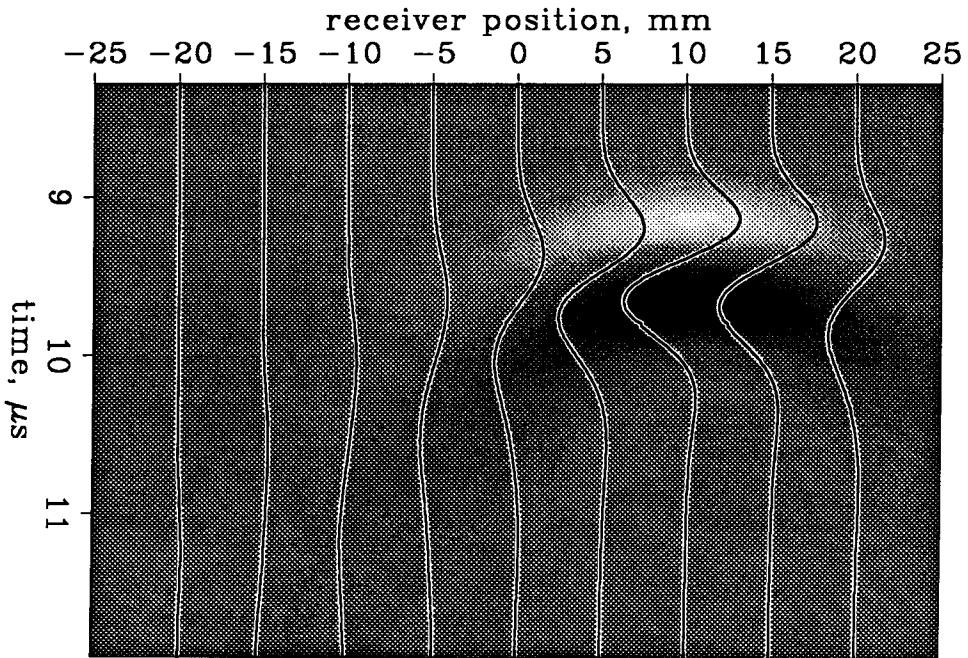
P source, layers at 45°

SV source, layers at 45°

FIG. 2.13. A simulation of waves propagating in a shale core sample, the same shale as in Figure 2.12. This time, however, the layers run from the lower left to the upper right (a 45° clockwise rotation from Figure 2.12). The dotted line shows the theoretical impulse-response surface for a point source at the center of the source transducer. Note the bulk of the qP energy misses the receiver transducer at the top of the core! The SV source and receiver transducers are bigger than the P ones, even though the qSV wave happens to still be well behaved even at 45°.
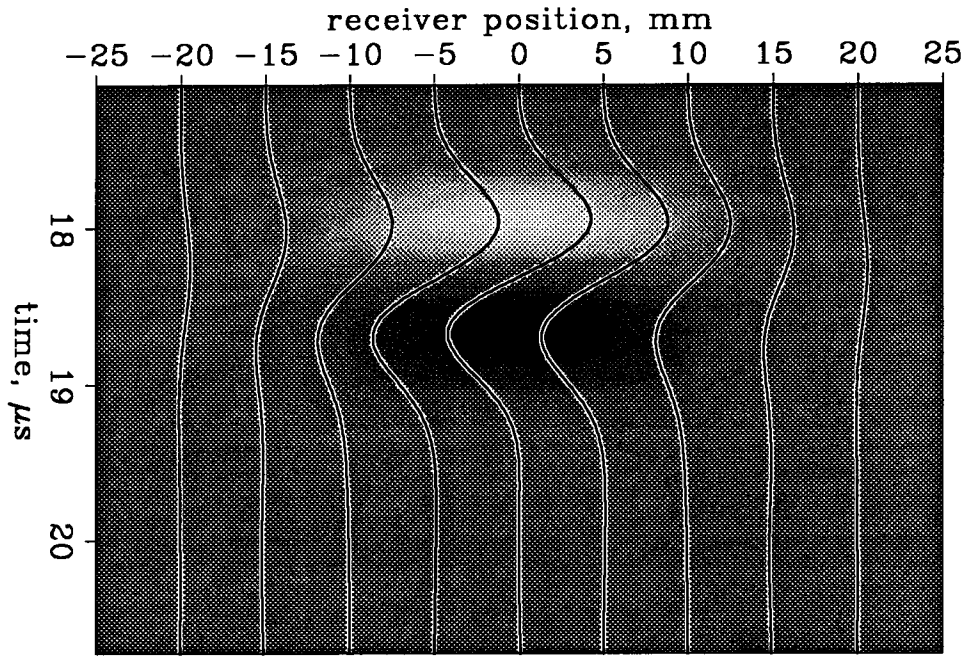
receiver position, mm

-25 -20 -15 -10 -5 0 5 10 15 20 25

time, μs
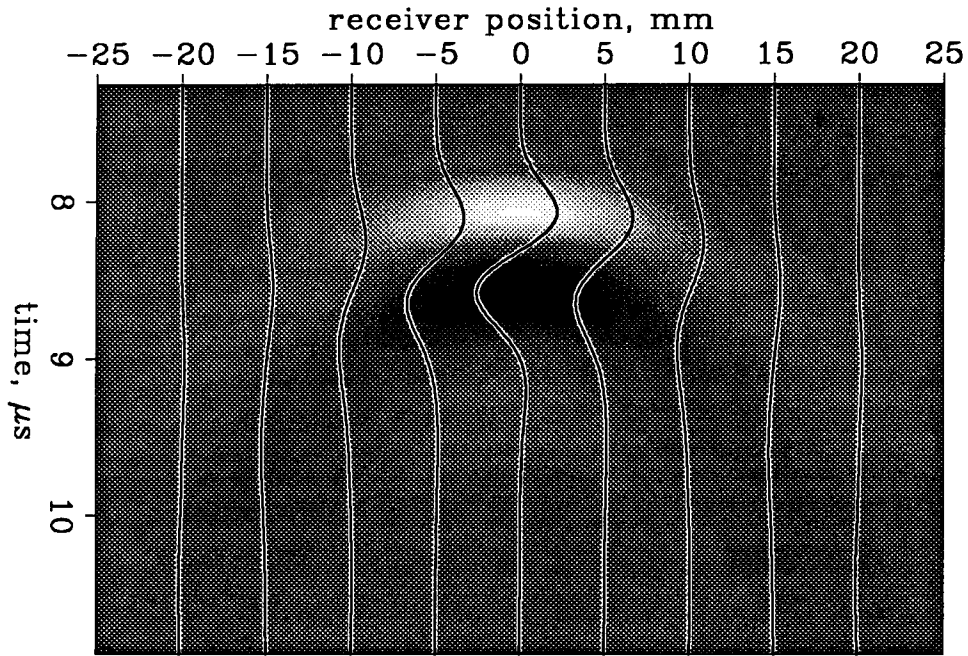
P signal, layers at 90°

receiver position, mm

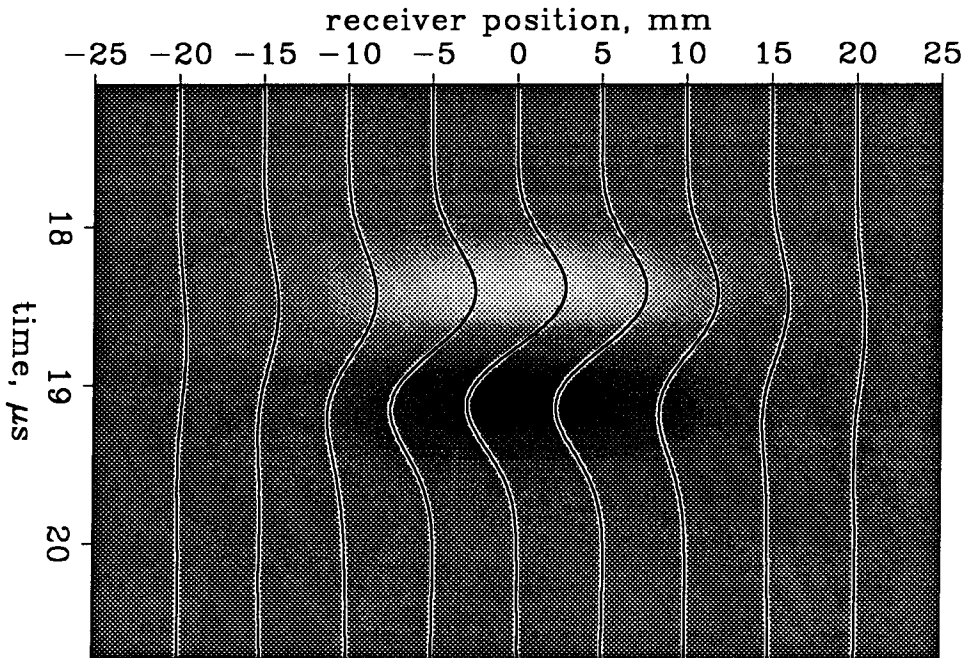-25 -20 -15 -10 -5 0 5 10 15 20 25

time, μs

P signal, layers at 45°

FIG. 2.14. Modeled P-wave sections for the two shale orientations, taking into account the extent of both the source and receiver P-wave transducers. The position of the receiver transducer is given by the horizontal axis, in millimeters; the source transducer is held fixed. A sample seismogram is shown every 5 millimeters. For the 45° case, the phase velocity (which must be determined at the point where the event arrives first) should have been measured from the seismogram shifted 10 millimeters to the right, not from the center.

FIG. 2.15. Modeled S-wave sections for the two shale orientations, taking into account the extent of both the source and receiver S-wave transducers. The position of the receiver transducer is given by the horizontal axis, in millimeters; the source transducer is held fixed. A sample seismogram is shown every 5 millimeters. The central position of the transducer accurately measures the phase velocity for both shale orientations.

Figure 2.11 shows the qP-qSV impulse-response surface for one of Vernik's more troublesome cores. Note that the qP wave for this medium is highly anisotropic (although not very exotic, being nearly perfectly elliptical). Figure 2.12 shows a snapshot of modeled qP and qSV waves propagating in a 90°-cut core made of this medium. (My model is two-dimensional, and lacks any free surfaces, but is sufficient to illustrate the point.) Since this orients the vertical source-receiver line along one of the symmetry axes, the group and phase velocities and directions are the same for this case. The waves proceed directly from one transducer to the other; the widths of the transducers are pretty much irrelevant.

Figure 2.13 shows what happens when the core is instead cut at a 45° angle to the layering. The 45° angle has no special symmetry, and so the group and phase directions are not the same. As we can see, the qP wave slips "sideways" all the way over to the right edge of the core by the time it makes it to the top. The bulk of the wave's energy almost completely misses the P receiver transducer! In the real core there would also be significant energy bouncing off the sides of the sample and contaminating the direct arrival. This probably explains why Vernik noticed such a weak and indistinct signal.

Figure 2.14 shows modeled P-wave sections for the two shale orientations. The position of the receiver transducer is given by the horizontal axis; the source transducer is held fixed. The measured phase velocity for the 45° case is about 3% low, and the amplitude is about 2.5 times too small. This error may not be too serious; Jones and Wang (1981) report a basic measurement accuracy on the order of 2% for P waves in their laboratory studies. Still, it is better to eliminate known sources of measurement error when possible.

What about the qSV waves? In the exotic examples in the previous subsection we saw that qSV waves are much more likely to misbehave than the relatively boring qP waves. Surprisingly enough, in Figure 2.13 the qSV wave is the better behaved of the two wavetypes shown. This is not a special characteristic of this medium; qSV waves often display a near symmetry about the 45° angle, something we might expect given that the vertical and horizontal velocities (both controlled by C_{55}) are the same. As a result the group and phase directions only differ by a few degrees for the 45°-cut case, not enough to cause a problem.

Figure 2.15 shows modeled S-wave sections for the two shale orientations. As expected, for both orientations the receiver accurately records the desired qSV phase velocity. It is ironic that the S transducer is also almost twice the width of the P transducer; the

measurements would have been better if it had been the other way around.

FIG. 2.16. The qP-qSV impulse-response surface for Bakken shale core sample #10164 (Vernik and Nur, 1990); the elastic constants are listed in Table C.1. The dotted lines are best-fitting 90° paraxial ellipses. The 45° line shows the direction of "vertical" in Figure 2.17.
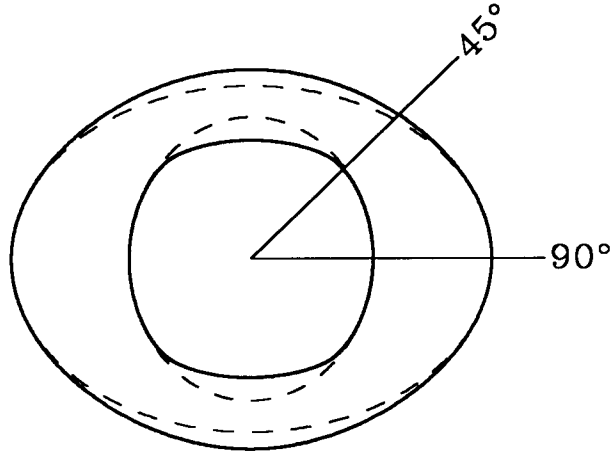

The models in the previous figures were based on one of Vernik's most strongly anisotropic shale cores; what about more typical examples? Figure 2.16 shows a typical core from the same formation. The P-wave anisotropy for this core is 23%, 1.5 times less than the P-wave anisotropy in the previous example. The qSV wave is somewhat more anisotropic, however. Figure 2.17 shows how the waves propagate in a 45°-cut core of this "typical" medium. As before, the bulk of the qP wave's energy misses the top transducer. This time the qSV wave is perceptibly shifted, but still not enough to cause any problem.

The actual situation is likely to be worse than that depicted here. My models are two dimensional and lack any boundaries. The qP waves in reality should be reflecting and focusing off the cylindrical free surfaces at the sides of the core, further complicating the situation. I also neglected to model the SH waves. For these two cores their anisotropy is about the same as that of the corresponding qP waves, although the situation is somewhat improved by virtue of the larger S source size.

2.4.3 What should TI look like?

In the previous subsections I have shown theoretical and laboratory examples. In this subsection I will show some of the ways that two-dimensional anisotropy might affect standard isotropic geophysical techniques.
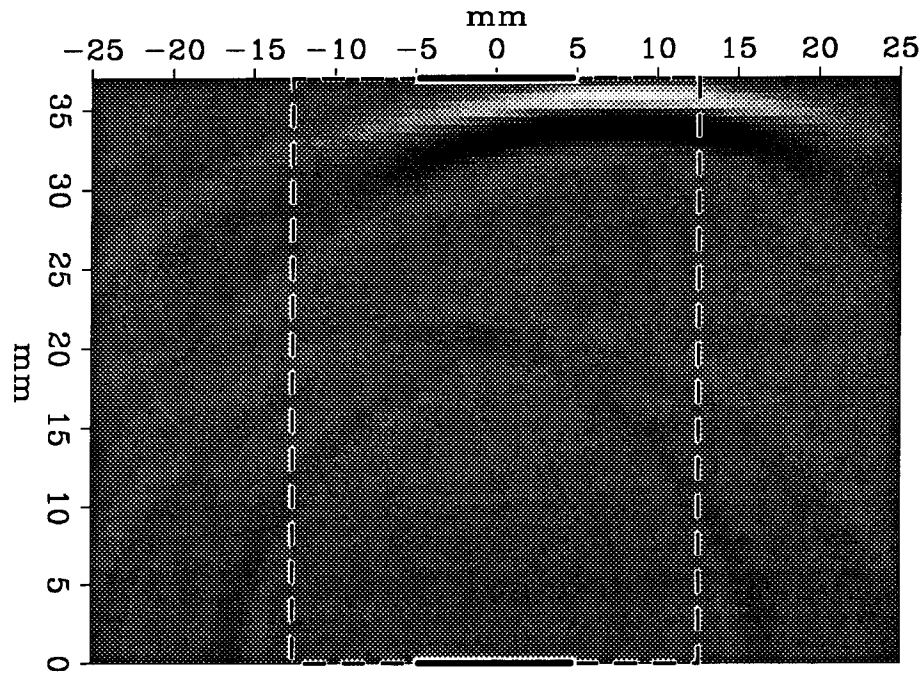
P source, layers at 45°
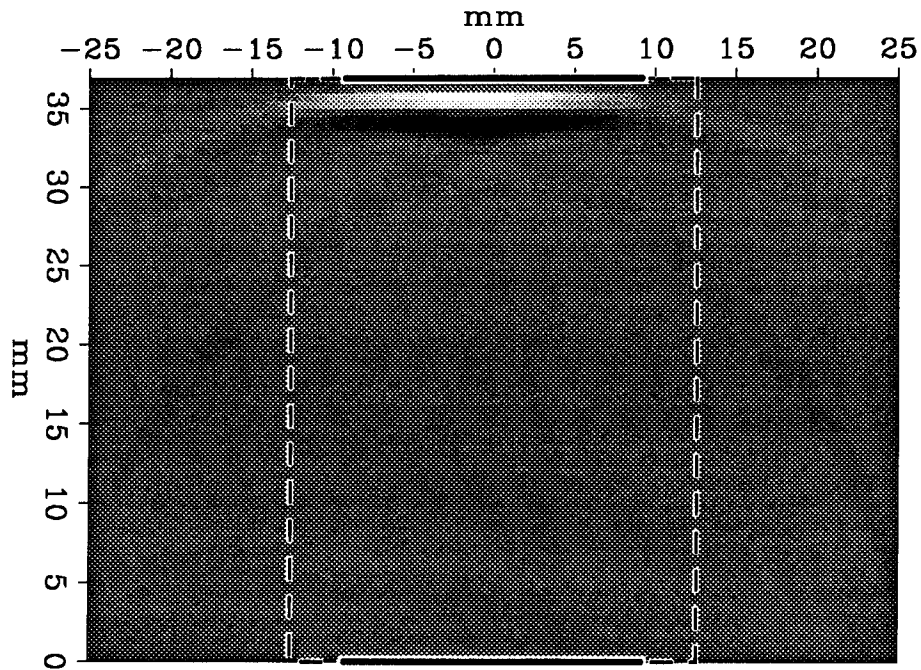
SV source, layers at 45°

FIG. 2.17. A simulation of waves propagating in a shale core sample. The layers in the shale run from the lower left to the upper right. The outlines of the core sample are shown by the dotted line. The position and size of the source (at bottom of core) and receiver (at top) transducers are shown by the heavy black lines. The source has a dominant frequency of .956MHz, the vertical P velocity is 4.22 km/sec, and the upper snapshot is at 9.66 μsec and the lower is at 15.69 μsec.

Time-to-depth conversion

As we already saw in section 2.1.2, elliptical anisotropy preserves hyperbolic moveout but causes errors in time-to-depth conversion. How would this work in practice?

FIG. 2.18. The elliptical qP and qSV wavefronts for the medium already shown in Figure 2.4, #5. The vertical (time-to-depth) qP velocity is 3.048 km/sec, and the horizontal (NMO) velocity is 3.736 km/sec. Both the vertical and horizontal qSV velocities are 1.490 km/sec.
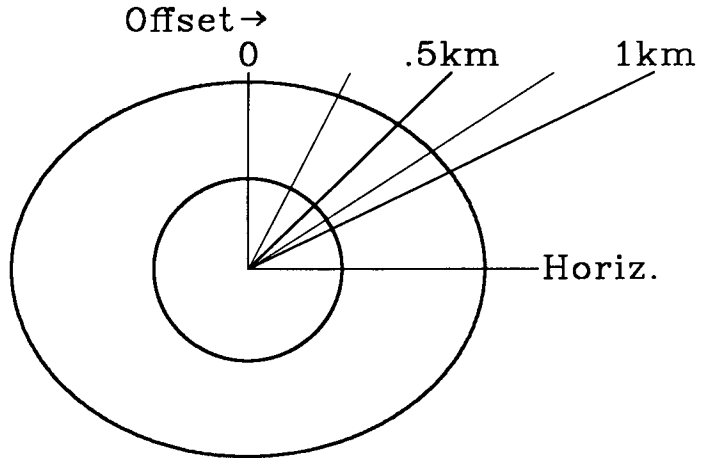
Figure 2.18 shows the qP-qSV impulse-response surface for a TI medium with elliptical wavefronts. Figure 2.19 shows how NMO would work in a section recorded over a homogeneous half-space of this medium. Since the wavefronts are elliptical, the events in the section are hyperbolic and standard NMO correctly flattens them.

We can get into trouble if we try to use these NMO velocities directly for time-to-depth conversion. For the qSV wave the horizontal and vertical velocities happen to be the same in this example, and so from that event we determine the correct source depth of 500 meters. For the qP wave, however, the NMO velocity is 3.736 km/sec, 22% larger than the vertical time-to-depth velocity. As a result we calculate a source depth of 613 meters, over 100 meters too deep. Such qP-qS depth misties are often reported in the literature (for example Winterstein (1986), although he looks at qP and SH waves).

Non-hyperbolicity

What if we have a more general transversely isotropic medium, one with non-elliptical wavefronts? Figure 2.20 shows such a medium. Although the wavefronts are not elliptical, it is possible to fit an ellipse to the wavefronts very accurately for near-vertical propagation, corresponding to near offsets in the survey.

x position, km

Elliptic, Zx, d=500m
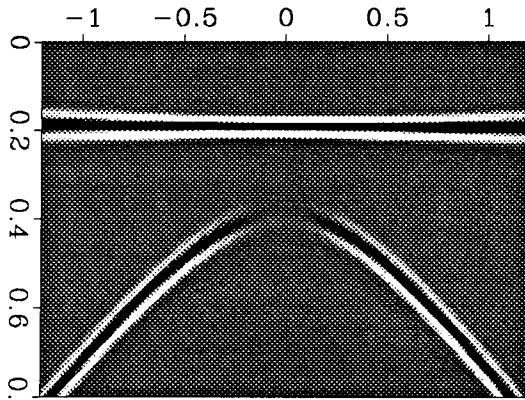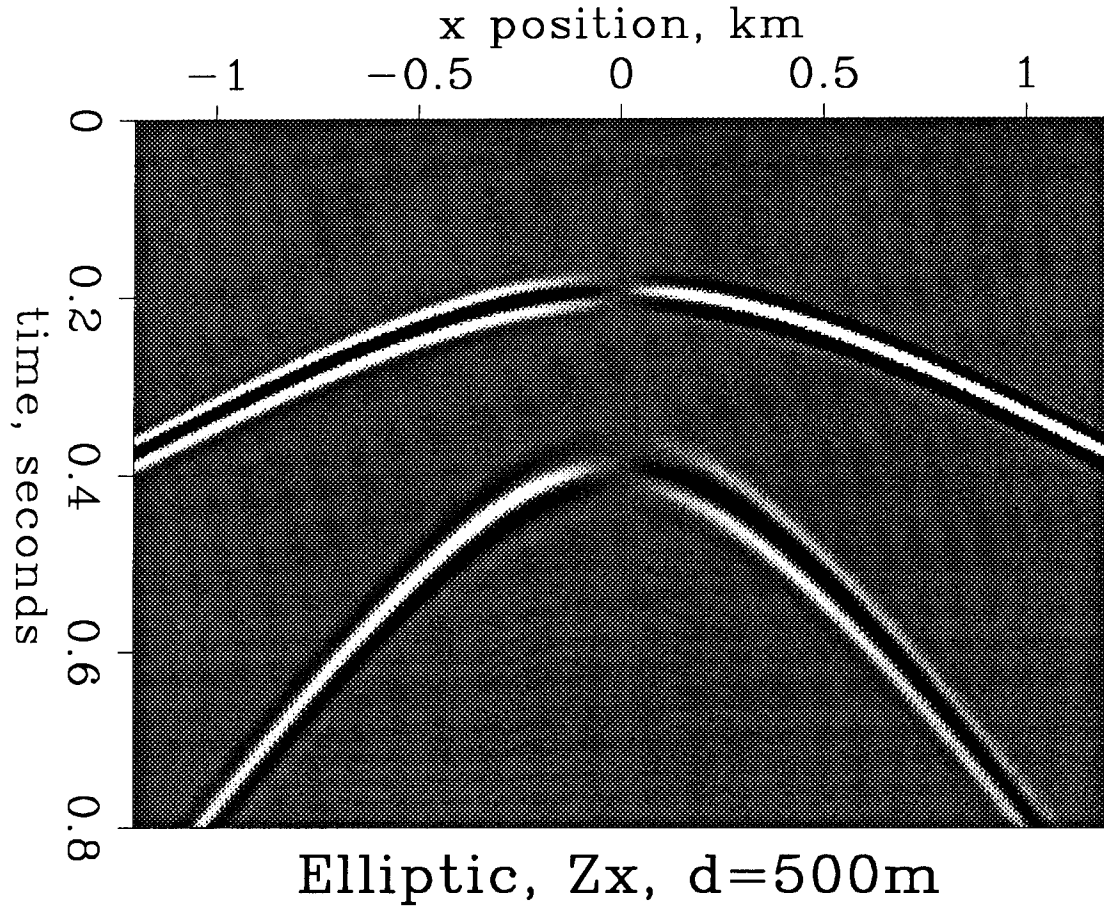
P—NMO, Zz, v=3.736
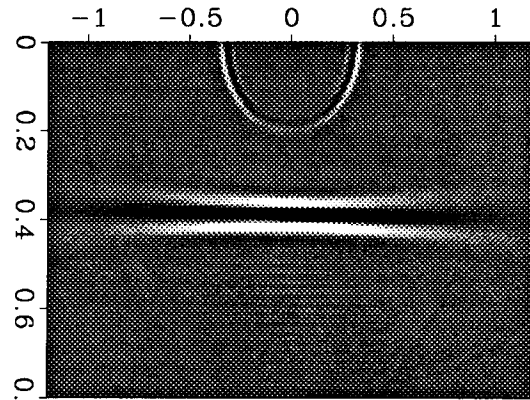
S—NMO, Xx, v=1.490

FIG. 2.19. Model section recorded over a homogeneous block of the medium shown in Figure 2.18. The source is a point force buried at 500 meters. Top: Z source into x receivers, showing the hyperbolic qP and qSV arrivals. Bottom left: Z source into z receivers, moved-out with the horizontal qP velocity. Bottom right: X source into x receivers, moved-out with the horizontal qS velocity.

FIG. 2.20. The non-elliptical
qP and qSV wavefronts for the
medium already shown in Fig-
ure 2.4, #3. The vertical
and horizontal velocities for both
wavetypes are the same as for the
medium in Figure 2.18. The dot-
ted lines show the
best-fitting near-vertical paraxial
ellipses. The horizontal velocities
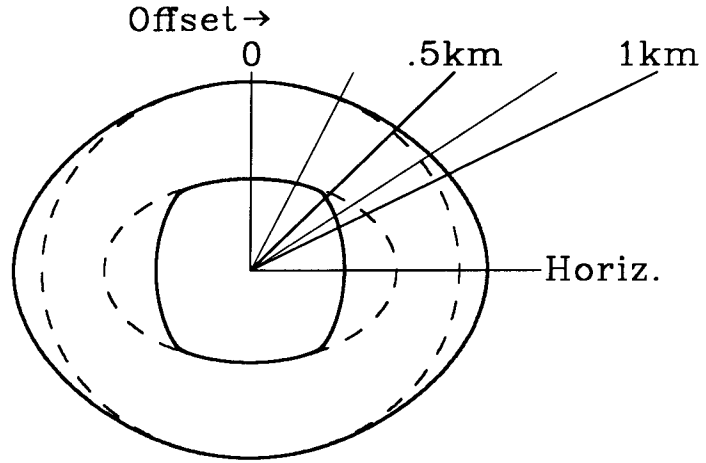on these ellipses determine the
corresponding near-offset NMO
velocities.

Figure 2.21 shows how moveout works in such cases. (Uren, Gardner, and McDon-
ald (1990) show t^2-x^2 plots and raypaths for similar non-hyperbolic examples.) The ve-
locities suitable for the near offsets fail for the outer ones, especially for the qSV event.
The near-offset moveout velocities have very little relation to the true horizontal and ver-
tical velocities. For example, using the best-fitting qSV NMO velocity of 2.313 km/sec we
would calculate a source depth of 776 meters, a whopping 55% error!

AVO

If anisotropy is present it should also be taken into account when looking for amplitude-
versus-offset effects. Figure 2.22 shows how the amplitude of the qSV wave in the previous
example has huge amplitude variations near the incipient triplications.

Raypaths

Although I won't show any examples, this is also the place to mention that when dealing
with anisotropy one must be very careful about assuming the properties of raypaths.
Dellinger (1989), for example, demonstrates a model where rays crossing a planar interface
from an isotropic medium into a transversely isotropic one bend towards the normal, even
though the anisotropic medium they are entering is faster for all directions of propagation.
Shearer and Chapman (1988) present an excellent rogue's gallery of raypaths in gradient
media. Instead of following well behaved circles as in the isotropic case, the rays often
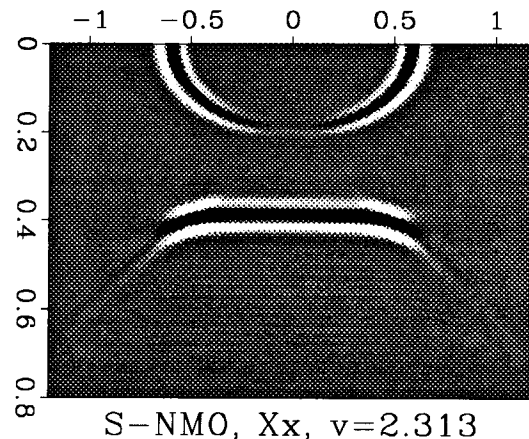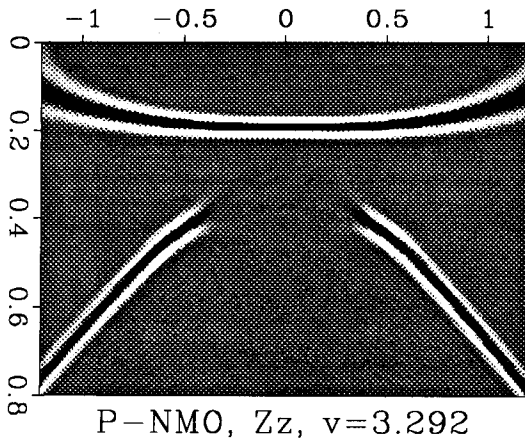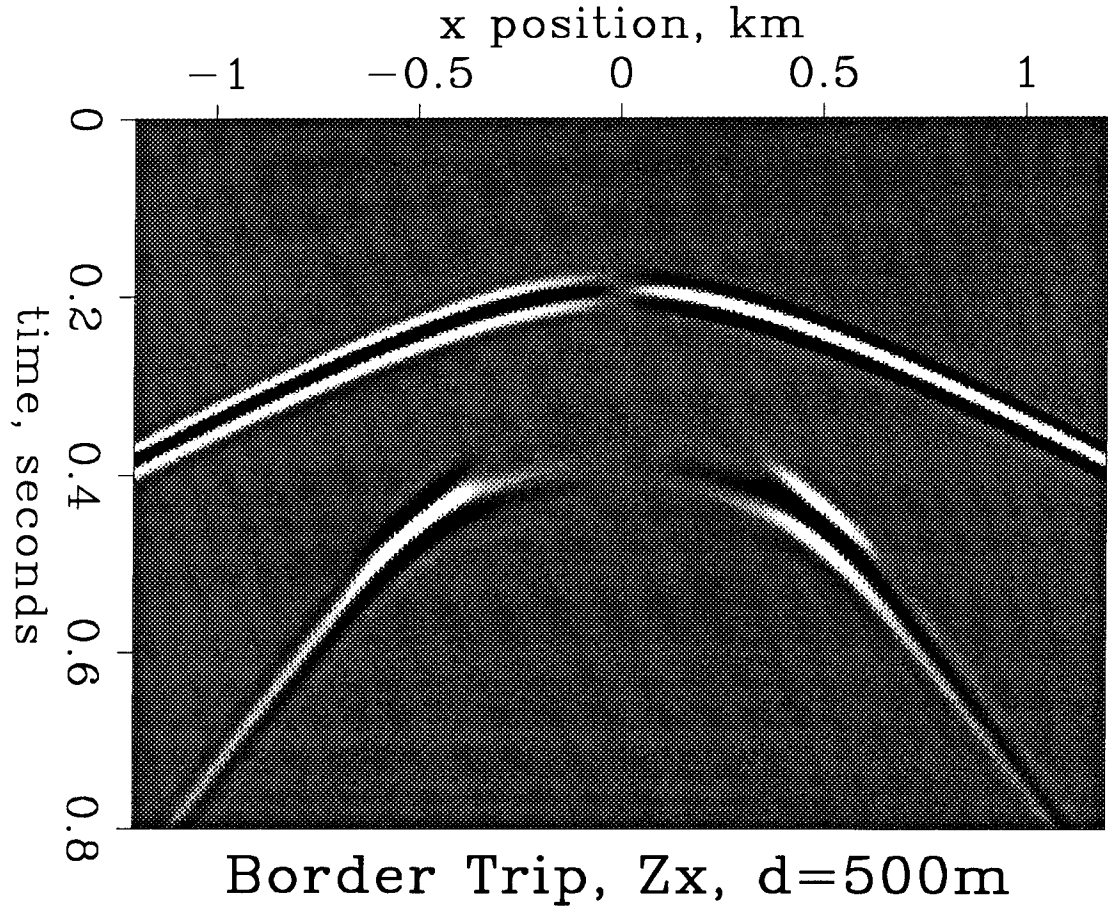
FIG. 2.21. Model section recorded over a homogeneous block of the medium shown in Figure 2.20. The source is a point force buried at 500 meters. Top: Z source into x receivers, showing the qP and qSV arrivals. Bottom left: Z source into z receivers, moved-out with the best-fitting qP NMO velocity for small offsets. Bottom right: X source into x receivers, moved-out with the best-fitting qS NMO velocity for small offsets.
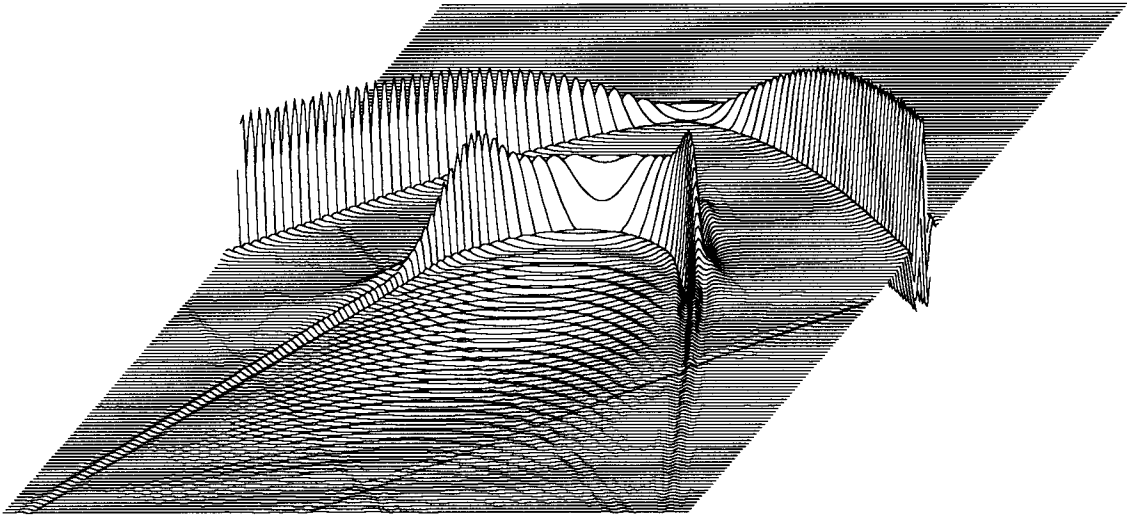
FIG. 2.22. Another view of the data in the bottom-right plot in Figure 2.21, showing the large amplitude variations versus offset on the qSV wave caused by anisotropy. The data in this plot has not been moved out.

bob up and down several times before finally heading back up for good.

2.5 Wavetype separation in two dimensions[8]

So far in this chapter I have shown some of the theory of two-dimensional anisotropy and many finite-difference examples, some of which were extremely non-isotropic. Can standard algorithms be extended to include these sorts of distinctly non-isotropic wavefields? In this section I will show how to extend one of the most basic and useful operators, the divergence operator, to encompass general two-dimensional anisotropy.

2.5.1 Mode separation in two dimensions

Any arbitrary vector field $\mathbf{U}(x, y, z)$ can be expressed

$$\mathbf{U} = \nabla P - \nabla \times \mathbf{S}, \tag{2.23}$$

where P is a scalar and $\mathbf{S}$ is a vector field with zero divergence. If $\mathbf{U}$ is an isotropic wavefield, then P and $\mathbf{S}$ are called the P and S potentials, respectively (Aki and Richards,

---

[8]This section is modified from "Wave-field separation in two-dimensional anisotropic media" (Dellinger and Etgen, 1990) .

1980). In two dimensions $\mathbf{S} = S\mathbf{1}_z$, where S is a scalar and $\mathbf{1}_z$ is the unit vector $(0,0,1)$, so both P and $\mathbf{S}$ can be treated as scalars. Equation (2.23) is usually not used directly in practice. Instead a two-dimensional isotropic wavefield $\mathbf{U}$ is decomposed into P and S components by calculating $\nabla \cdot \mathbf{U}$ ($= \nabla^2 P$) and $\nabla \times \mathbf{U}$ ($= \mathbf{1}_z \nabla^2 S$) respectively. This wave separation property of $\nabla \cdot$ and $\nabla \times$ is commonly exploited by elastic inversion and migration algorithms to allow separate treatment of P and S waves.

The isotropic case: div and curl

Any vector wavefield, isotropic or not, can be split into two potentials via equation (2.23), but the resulting potentials only represent pure wavetypes in the isotropic case. Our goal is to separate qP and qS waves in *anisotropic* wavefields. We begin by showing how $\nabla \cdot$ extracts P waves in the standard isotropic case.

The divergence of a two-dimensional elastic wavefield $\mathbf{U}$ is

$$\nabla \cdot \mathbf{U} = \frac{\partial U_x(x,y)}{\partial x} + \frac{\partial U_y(x,y)}{\partial y}. \tag{2.24}$$

In the Fourier domain this is

$$\widehat{\nabla \cdot} \; \hat{\mathbf{U}} = i\,k_x\,\hat{U}_x(k_x,k_y) + i\,k_y\,\hat{U}_y(k_x,k_y), \tag{2.25}$$

where $\hat{\mathbf{U}}$ and $\widehat{\nabla \cdot}$ are the Fourier-domain representations of $\mathbf{U}$ and $\nabla \cdot$, respectively.

A more illuminating way to write equation (2.25) is

$$\widehat{\nabla \cdot} \; \hat{\mathbf{U}} = i\,k\,(\mathbf{l} \cdot \hat{\mathbf{U}}), \tag{2.26}$$

where $k = \sqrt{k_x^2 + k_y^2}$ is the wavenumber at (k_x, k_y) and $\mathbf{l}$ is the unit wave normal vector $(k_x/k, k_y/k)$ pointing in the direction of (k_x, k_y). Each point (k_x, k_y) in the Fourier domain represents plane waves traveling in the direction $\mathbf{l}$ with spatial frequency k. At any given (k_x, k_y) there are two wavetypes, distinguishable from each other by their distinct velocities and particle motion directions. In isotropic media the wavetypes are P and S, and the particle motions are simple: P waves shake along the direction of travel ($\parallel \mathbf{l}$), while S waves shake perpendicular to the direction of travel ($\perp \mathbf{l}$). Thus, the $\mathbf{l} \cdot \hat{\mathbf{U}}$ in equation (2.26) admits P waves (because the P particle motion is parallel to $\mathbf{l}$) but zeros S waves (because
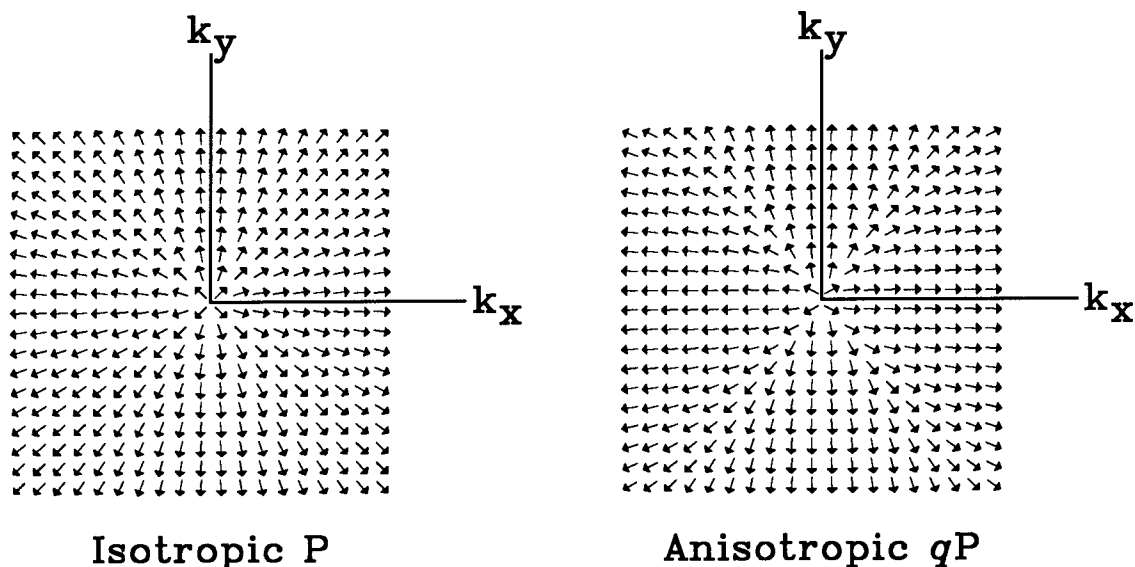
Isotropic P   **Anisotropic qP**

FIG. 2.23. Left: Fourier-domain plots of the operator for passing only P waves in isotropic media. Right: Fourier-domain plots of the operator for passing only P waves in the anisotropic medium used in Figure 2.24.

the S particle motion is orthogonal to l).

The divergence operator is not purely a wavetype separation operator because of the additional presence of the factor k. This factor acts like a derivative operator in the space domain, amplifying higher spatial frequencies. An operator that rejects S waves while passing P waves of all frequencies equally can be constructed by inverse Fourier transforming the operator

$$i \, \mathbf{l} \cdot \tag{2.27}$$

instead of the Fourier-domain divergence operator

$$\widehat{\nabla \cdot} = i \, k \, \mathbf{l} \cdot \tag{2.28}$$

appearing in equation (2.26). The left plot in Figure 2.23 shows a graphical Fourier-domain representation of the operator in equation (2.27). (In case you were wondering, the extraneous "i" in equation (2.27) keeps the operator real in the space domain; l is *anti*symmetric about the origin.)

If the operator in equation (2.27) is an ideal isotropic wave separation operator, why is

$\nabla \cdot$ (equation (2.28)) normally used instead? The problem is that $i\, \mathbf{l} \cdot$ is discontinuous at $(k_x = 0, k_y = 0)$, where $\mathbf{l}$ becomes undefined. This discontinuity is not automatically fatal, because wavefields typically have no energy at zero frequency anyway. Unfortunately, the discontinuity at $(k_x = 0, k_y = 0)$ in the Fourier domain also means the operator $i\, \mathbf{l} \cdot$ has tails extending off to infinity in the space domain. It is thus less compact than the divergence operator, which is a point differential operator in the space domain.

Extending to anisotropy

Our isotropic wavetype separation theory generalizes to the anisotropic case in an obvious way. The principal change is that the particle motion directions of the wave modes are no longer simply $\parallel \mathbf{l}$ or $\perp \mathbf{l}$; instead the particle motion directions may be complicated functions of k_x and k_y. In the Fourier domain the anisotropic wavetype separation operator has the form $i\, \mathbf{v}(k_x, k_y) \cdot$, where $\mathbf{v}(k_x, k_y)$ is a unit vector giving the particle motion direction of the desired mode on the plane wave (k_x, k_y).

How do we find the required particle motion directions? Fourier transformation separates wave fields by their plane-wave components. The Christoffel equation is just the elastic wave equation Fourier transformed over space and time. The required particle motion directions can thus be found from equation (2.4), the general three-dimensional Christoffel equation.

We are only interested in the simpler two-dimensional case here, so we can discard the y variable. This simplifies equation (2.4) to

$$\underset{\sim}{\mathbf{D}}\, \underset{\sim}{\mathbf{C}}\, \underset{\sim}{\mathbf{D}}^T\, \mathbf{v}_n = -\rho \Big(\frac{\omega_n}{k}\Big)^2 \mathbf{v}_n \quad ,$$

$$\underset{\sim}{\mathbf{D}} = \begin{bmatrix} l_x & 0 & l_z \\ 0 & l_z & l_x \end{bmatrix} \quad , \tag{2.29}$$

and

$$\underset{\sim}{\mathbf{C}} = \begin{bmatrix} C_{11} & C_{13} & C_{15} \\ C_{13} & C_{33} & C_{35} \\ C_{15} & C_{35} & C_{55} \end{bmatrix} \quad ,$$

where $\underset{\sim}{\mathbf{D}}$ is a matrix involving only $\mathbf{l}$, $\underset{\sim}{\mathbf{C}}$ is the stiffness matrix that defines the elastic properties of the medium, ρ is the density of the medium, ω_n is the temporal frequency for

solution n, k is the spatial wavenumber, and v_n is the associated particle motion direction (Auld, 1973). For a given $\underset{\sim}{C}$, k, and l, equation (2.29) always has two orthonormal solutions v_1 and v_2. Each of these solutions corresponds to one wavetype.

Algorithm description

Now we have everything we need to extend our isotropic wave separation algorithm to handle anisotropy:[9]

(1.) Decide which mode ("quasi-P or quasi-S") this operator will pass.

(2.) For all (k_x, k_y):

{

(A.) Substitute k_x and k_y into equation (2.29) and find the two solutions v_1 and v_2.

(B.) Decide whether solution 1 or 2 corresponds to the desired mode chosen in step (1). Call this solution v.

(C.) Both v and $-v$ are equally valid normalized solutions. Choose the one that is consistent with particle motion directions already determined at adjacent (k_x, k_y) points.

(D.) Store the result for this (k_x, k_y) in $V(k_x, k_y)$.

}

(3.) Inverse Fourier transform the operator i $V\cdot$, obtaining the desired (x, y)-domain wave separation operator.

In practice compactness of the operator in the space domain is desirable. There are two Fourier domain discontinuities to avoid, at the origin and the Nyquist. The first can be removed by multiplying the operator by k, following the example of the divergence operator. The second can be avoided by a suitable Fourier domain window function.

---

[9]If it occurs to you that this algorithm is incomplete because I really didn't explain step 2B, and that there is no guarantee a consistent sign choice is possible at step 2C, you are right! However, as we will prove in section 3.2.3, things work here despite our lack of rigor.

2.5.2 Examples

To demonstrate the method, I generated a wavefield using a finite-difference elastic modeling program. The model is split into three parts: an upper left part, an upper right part, and a bottom part. The upper left part is isotropic, and the upper right part is anisotropic. (The elastic constants are listed in Table C.1 in Appendix C.) These two media were chosen to have the same vertical velocities. The bottom part of the model grades uniformly from the isotropic elastic constants at the left edge to the anisotropic ones at the right edge. The density is uniform throughout.

The left plot in Figure 2.23 shows the P wavefield separation operator appropriate for the isotropic elastic constants. The right plot in Figure 2.23 shows the P wavefield separation operator appropriate for the anisotropic elastic constants. To avoid the Fourier-domain discontinuities at the origin and Nyquist, we also incorporated a derivative (k) and a raised cosine taper ($.5(1 + \cos(\pi \; k/k_{\text{Nyquist}}))$) in our wavetype separation program.

Figure 2.24 shows the results of applying operators appropriate for each set of elastic constants to the whole. The top two plots in the figure show the input wavefield, which contains complicated interacting wavefronts of both wavetypes. If the separation operators work correctly, they should admit one wavetype while exactly zeroing the other. Examining the figure, we can see that each set of operators works well in the appropriate part of the medium: the isotropic operators work in the upper left block, and the anisotropic operators work in the upper right block. The separations are not quite perfect because of slight numerical anisotropy in the finite-difference modeling program; a small amount of the undesired wavetype does get through (about 1%). As expected, none of the separations work very well in the central portion of the lower block, where neither set of operators is appropriate.

2.5.3 Discussion

Heterogeneous media

Another kind of error is visible along the bottom edges of the lower 4 plots in Figure 2.24 (the arrows point to one example). The wavetype-separation operators were applied in the Fourier domain with no padding. To the operators the model is thus cyclic, and the free surface at the top of the model abuts directly against the absorbing boundary at the bottom. This creates both a heterogeneity in the elastic constants and a discontinuity in

Original Wavefield, X comp.

Original Wavefield, Z comp.

Isotropic P

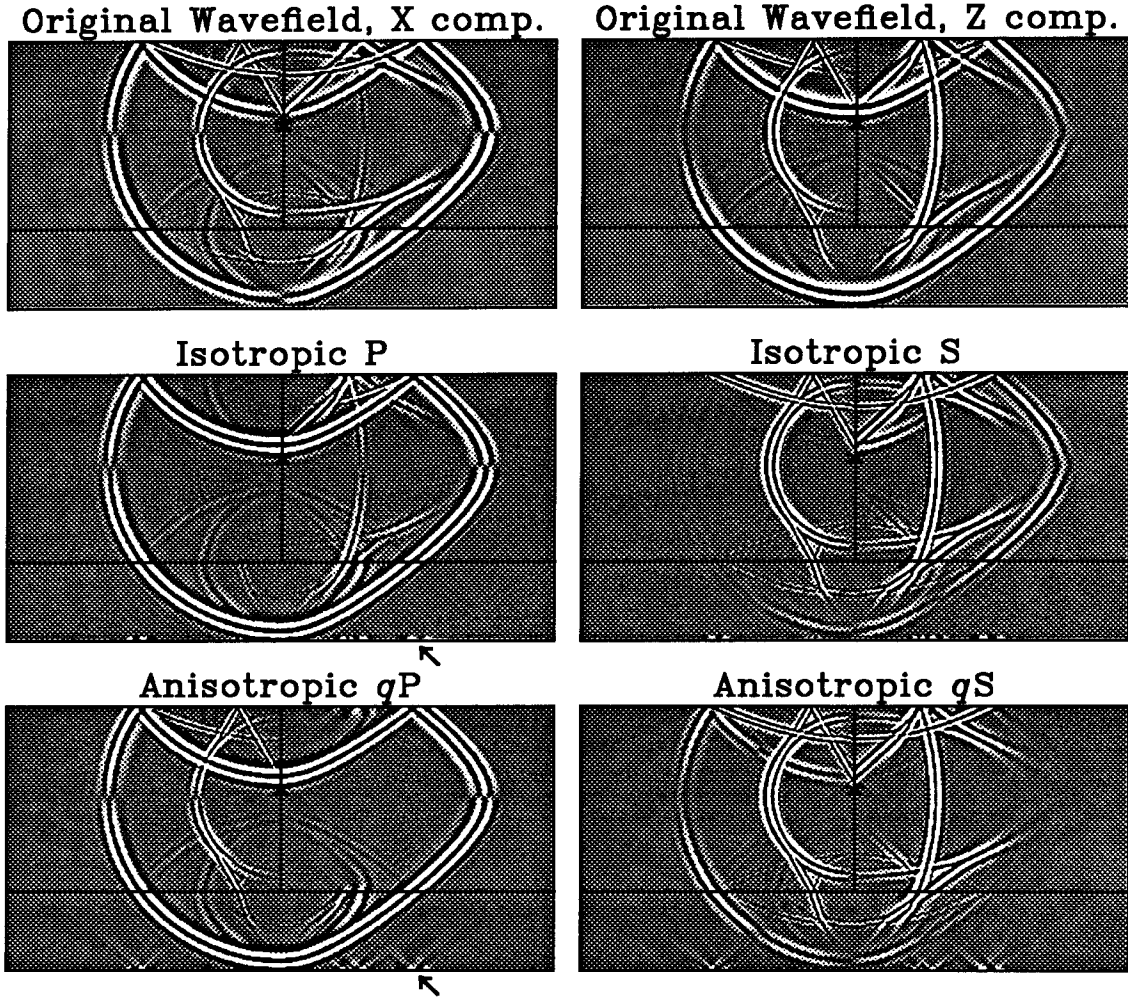## Isotropic S

Anisotropic qP

Anisotropic qS

FIG. 2.24. Top: Snapshot of the X (left) and Z (right) components of a finite-difference wavefield. The grid is 512 wide by 256 tall, with absorbing boundaries on the left, right, and bottom borders and a free surface boundary at the top. The model consists of two layers. The upper layer is divided into left and right halves. The left half is isotropic and the right half is anisotropic. Underneath is a single layer that grades smoothly from isotropic on the left to anisotropic on the right. The source is a vertical impulsive point force at the "×". Middle: The result of applying isotropic wavefield separation operators (divergence and curl) to the entire medium; the separation works in the upper left block. Bottom: The result of applying anisotropic wavefield separation operators to the entire medium; the separation works in the upper right block. The lower four plots are all plotted with the same parameters; square root amplitude gain and heavy clipping have been applied to make weak events and artifacts visible.

the wavefield itself.

Since the operators were derived assuming a uniform homogeneous medium, it is not clear how well they should work across free surfaces and other such elastic-constant heterogeneities. The most important factor is how compact the operators are in the space domain; a compact operator is more tolerant of heterogeneities of any kind. Figure 2.25 shows a close up of the impulse response of the discretized isotropic and anisotropic wave separation operators. The discretized isotropic operator shown is relatively compact, while the anisotropic operator possesses "tails" extending out from the center of the operator. The arrows below two of the plots in Figure 2.24 point to the same free surface wraparound artifact for the isotropic and anisotropic cases. As we expected from Figure 2.25, in the isotropic case the artifact is much smaller.

We know that in the continuous limit, the isotropic operators collapse to the point differential operators divergence and curl. We cannot expect such a collapse to happen for arbitrary operators defined in the Fourier domain, any more than we can expect the one-dimensional Fourier transform of some general function to collapse to a point. The tails of the discrete anisotropic wave separation operator in Figure 2.25 are a warning that in the continuous limit anisotropic wave separation operators are probably not normally point differential operators like divergence and curl.

While disturbing in theory, such tails should not be much of a problem in practice. Even in the extremely anisotropic "worst case" example in Figure 2.24, the tails are only noticeable along the large discontinuity at the top and bottom of the model. The amplitude of the artifacts there is only a few percent of the amplitude of the waves reflecting at the free surface.

Do we really need the elastic constants?

We know that for isotropic media $\nabla\cdot$ separates the two wavetypes regardless of the density, P velocity, or S velocity. Equation (2.29), on the other hand, seems to require complete knowledge of both the elastic constants and density. Are the anisotropic and isotropic cases somehow fundamentally different? No. Equation (2.29) solves for both the particle motion directions $\mathbf{v}_n$ and the phase velocities ω_n/k for each mode, but for the purpose of separating wavetypes only the particle motion direction matters. This gives us some latitude in specifying the medium. For example, the value of ρ is clearly irrelevant, since it scales the phase velocities but has no effect on the particle motion directions. Likewise,
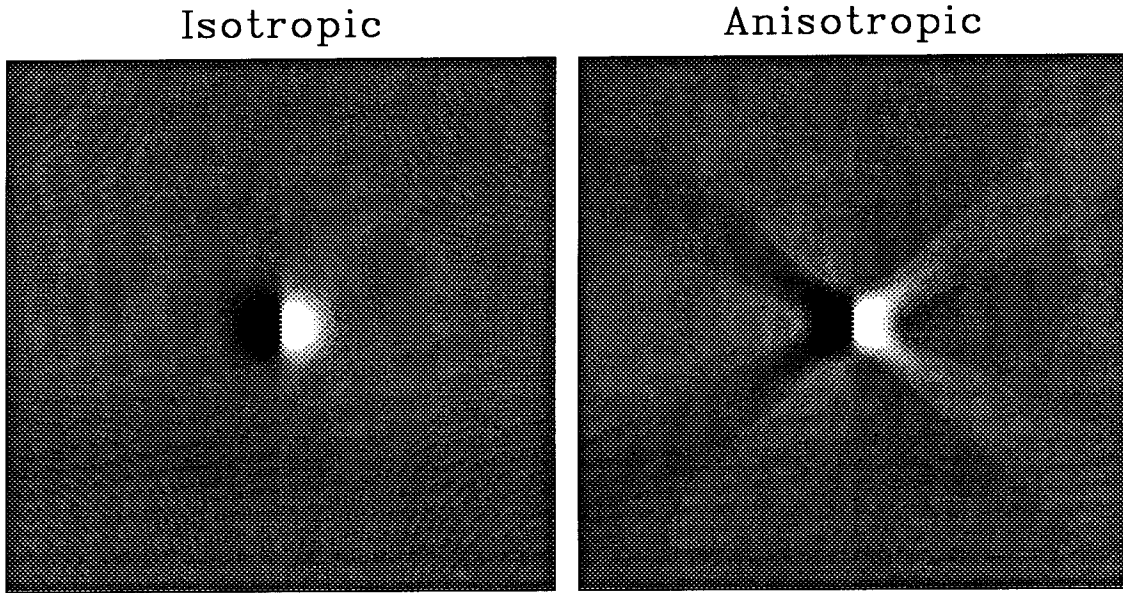
Isotropic

Anisotropic

FIG. 2.25. P wavetype-separation operator impulse responses for the isotropic and aniso-tropic media in Figure 2.24. The operators were calculated on a 2048^2 grid using a smoothed vertical impulse source. A 201^2 subgrid centered on the impulse is shown. Both plots are plotted with the same parameters; as in Figure 2.24 square root amplitude gain and heavy clipping have been applied to make low amplitude features visible. The isotropic operator is clearly more compact than the anisotropic one, although the "tails" of the anisotropic operator are at most a few percent of the amplitude of the central spike.

the stiffness matrix $\underset{\sim}{C}$ can be freely scaled up and down.

In the isotropic case there is one more degree of freedom, so we expect there should be one more in the anisotropic case as well. For qP and qSV waves in transverse isotropic media the transformation

$$C_{33} + \Delta C \implies C_{33},$$

$$C_{11} + \Delta C \implies C_{11},$$

$$C_{55} + \Delta C \implies C_{55}, \tag{2.30}$$

and

$$C_{13} - \Delta C \implies C_{13}$$

has no effect on the particle motion directions for any legal value of ΔC, and thus no effect on the corresponding wavetype-separation operator. This last degree of freedom in $\underset{\sim}{C}$ can radically change the shapes of the wave surfaces, however.

Figure 2.26 shows an example of wavetype separation in an anisotropic strongly heterogeneous finite-difference model. The same wavetype-separation operator is appropriate in all three parts of the model. The lower left part is normalized "Greenhorn Shale" (Jones and Wang, 1981). The medium in the lower right part has the same density, particle motion direction and vertical qP velocity as "Greenhorn Shale", but radically different qS behavior. Finally, the upper part of the model grades linearly between the two sets of elastic constants from one edge to the other, and has a constant density 1.2 times the density of the lower two blocks. Note that the same operator works perfectly in both of the lower parts of the model. It does appear to have some trouble in the upper continuously varying medium, where the underlying homogeneous assumption breaks down. The "qS" component shown leaking through is really there, though: it is actually an evanescent qP wave converting from the qS wave as the qS wave encounters the (continuous) heterogeneity.

Is it useful?

We have shown it is possible to separate anisotropic wavetypes in time snapshots if the elastic constants are known. This type of wavetype separation should be applicable in elastic migration or inversion algorithms, where it allows one to examine contributions to the image due to different reflected and converted waves separately. For example, by correlating upcoming qSV waves with downgoing qP waves we obtain the qP-qSV reflection amplitude any place the waves overlap in space and time (Claerbout, 1985). By treating the various possible reflected waves separately, we should be able to better estimate changes in material parameters across interfaces.

Wavetype separation requiring time snapshots and known elastic constants is not directly useful for separating P and S arrivals in surface seismic data or VSP's. We do not record time snapshots $(x, z, t = \text{const})$ in the field, and we do not normally know elastic constants.

The first objection need not be fatal; techniques such as reverse-time migration can be used to reconstruct time snapshots from field data. Alternatively, we can adapt the algorithm to the recording geometry. For VSP data, for example, if we know the elastic
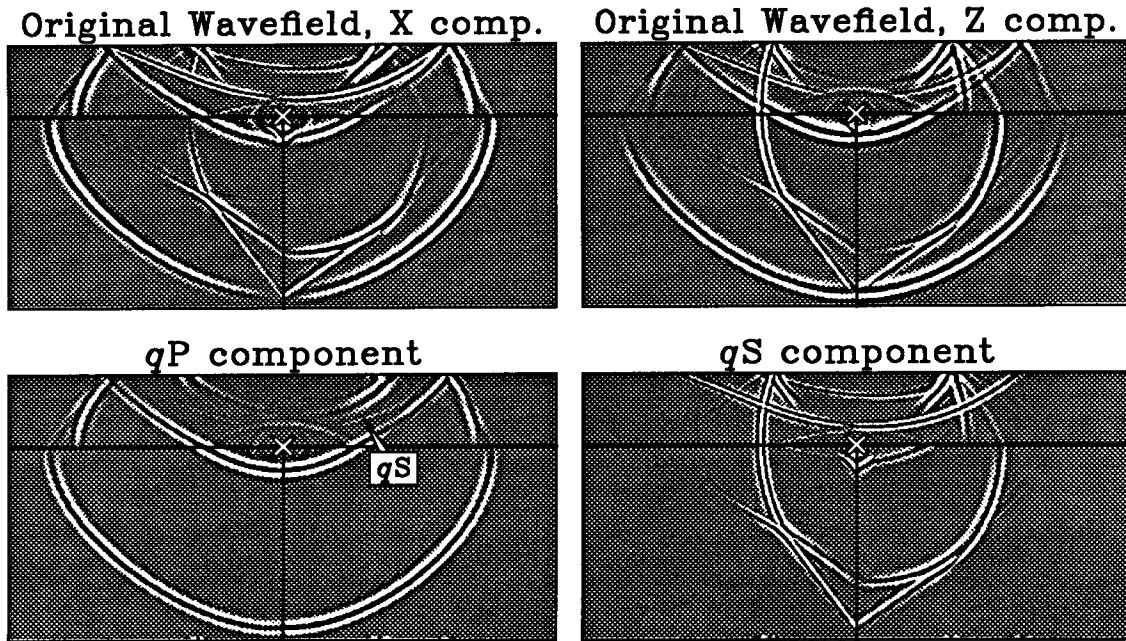
FIG. 2.26. Top: Snapshot of the X (left) and Z (right) components of a finite-difference wavefield. The differencing grid and boundary conditions are the same as those in Figure 2.24. The source is a vertical impulse point force at the "×". Bottom: The result of applying anisotropic wavefield separation operators to the entire medium. The separation works well everywhere, except for a small amount of qS that appears in the separated qP component. Hard clipping has been applied to make weak events and artifacts more visible.

constants we can solve for k_x as a function of k_z and ω, and perform the separation in the (k_z, ω) domain. This allows us to use VSP data of the form $(x = \text{const}, z, t)$. Devaney and Oristaglio (1986) show how to do this in the continuous isotropic case. For surface data we can similarly solve for k_z as a function of k_x and ω, and use surface data of the form $(x, z = \text{const}, t)$. There is the additional complication in this case of allowing for the free surface. This should be possible if the elastic constants at the surface are known.

What if the elastic constants are not known? In theory it should be possible to set up an inverse problem, and use the particle motion directions of distinct wavefronts to determine the necessary elastic constants. The trick is we have to identify distinct single-wavetype wavefronts first. Otherwise, for example, we could reverse-time migrate surface data using any elastic constants we wanted, and exactly account for the data by treating each recorded arrival as a coincidental instantaneous overlap of a P and an S wave.

What about three dimensions?

Trying to extend this algorithm to three dimensions is the central topic of section 3.2; it proves to be a very good vehicle for illuminating the complexities and surprises of three-dimensional anisotropy.